REVIEWS

Design of Gas-Inducing Reactors

Ashwin W. Patwardhan and Jyeshtharaj B. Joshi*

Department of Chemical Technology, University of Mumbai, Matunga, Mumbai 400 019, India

A gas-inducing impeller enables efficient recycling of gas from the headspace into the liquid. Historically, these impellers were used for the first time in froth flotation machines. The various designs of gas-inducing impellers (including those used in froth flotation) could be classified into three categories, depending on the flow pattern coming into and leaving the impeller zone. These are denoted as type 11, type 12, and type 22 systems. The critical impeller speed for the onset of gas induction (N_{CG}) is governed by a balance between the velocity head generated by the impeller and the hydrostatic head above the impeller. A number of correlations (for types 11 and 22) are based on this balance (Bernoulli's equation). The rate of gas induction (Q_G) for the type 11 system can be accurately determined by equating the pressure difference (between the impeller zone and the headspace) generated by the impeller and the pressure drop required for the flow of gas. For type 22 systems, the correlations for Q_G are mainly empirical in nature. Correlations for the power consumption, fractional gas holdup, mass-transfer coefficient, and so forth are also available in the literature, although these studies on are not comprehensive. A process design algorithm has been presented for the design of gas-inducing impellers. The algorithm consists of the determination of the rate-controlling step, selection of geometry and the operating conditions, and an economic analysis to choose the optimum design. Guidelines have been given about the desired geometry of gas-inducing impellers for achieving different design objectives such as heat transfer, mass transfer, mixing, solid suspension, froth flotation, and so forth. It has been shown that the use of a gas-inducing impeller in a conventional stirred vessel can lead to a substantial increase in the productivity. It has been shown that the optimum geometry may not correspond to the maintenance of equal power consumption per unit volume, or equal tip speed on scale-up. Suggestions have been made for future work in this area.

1. Introduction

In chemical process industries, gas−liquid contacting (with or without solids) is one of the most important operations. In many of the cases, the per pass conversion of gas is fairly low. It is desirable to recycle the unreacted gas back to the reactor because the gas may be highly toxic or may pose safety problems. Typical examples include alkylation, ethoxylation, hydrogenation, chlorination, ammonolysis, oxidation, and so forth. A recent report (Roby and Kingsley, 1996) comments that several oxidation reactions that currently use air can be operated more efficiently using pure oxygen. Typical examples of this are production of adipic acid, low-molecular-weight aliphatic acids, production of terephthalic acid, and so forth. The worldwide production of these chemicals amounts to several million tonnes per year. Hence, the benefits of using pure oxygen in these cases are enormous. In such applications, it is undesirable to use an external gas compressor. Moreover, an external gas compressor means addition in the capital as well as operating expenditure. Dead end systems would be highly advantageous under these circumstances. In these systems, the unreacted gas escapes into the reactor headspace and is recycled internally without the need of an external gas compressor. Gas-inducing contactors (GIC), surface aerators (SA), plunging jet reactors (PJR), an ejector jet loop reactor (EJLR), and rotating biological contactors (RBC) are considered as dead end systems.

Historically, one of the earliest reported use of a gas-inducing impeller is in froth flotation. In such cases, the gas-inducing impeller eliminates the need for a sparger. Abrasive solids present in the flotation of the ore can cause wear of the sparger holes; the gangue material present in the ore can form a muddy solid residue and block the holes of the sparger. This has adverse effects on the performance of a sparger system. In such cases, gas-inducing impellers are favorable and they can adequately deliver the quantity of the gas required. Harris (1976) has written an excellent review of the flotation machines. This unit process has attracted much attention over the past several years. Arbiter and Harris (1962), Arbiter and Steininger (1965), Arbiter et al. (1969), Harris (1976), Harris and Mensah-Biney (1977), Harris et al. (1983), Harris and Khandrika (1985a,b), Harris (1986), Schubert and coworkers (Schubert and Bischofberger, 1978; Schubert, 1985), and Grainger-Allen (1970) have investigated the performance of various flotation machines. Their studies, mostly semiempirical, try to correlate the hydrody-

* To whom correspondence should be addressed. E-mail: jbj@udct.ernet.in. Fax: (091)-022-414 5614. Tel.: (091)-022-414 5616.

10.1021/ie970504e CCC: $18.00
Published on Web 12/03/1998

namic and performance characteristics of the flotation machines with the geometry of the system, physicochemical properties, and the operating conditions. Dimensionless numbers such as *Re*, *Fr*, *Fl*, N_P, *We*, *Sh*, and so forth are used for this purpose.

The main objective in froth flotation is to selectively capture the particles of a certain mineral of the ore on the surface of the bubbles. Therefore, it is necessary to generate a large surface area (fine bubbles) and also to control their size distribution for achieving high selectivity. During flotation various chemical agents such as collectors, activators, frothers, and so forth are added. These chemicals help to increase bubble−particle adhesion, activate the bubble surface, promote frothing action by preventing bubble coalescence, and so forth. The gas-inducing impeller has to generate fine bubbles to achieve a high interfacial area. The frothers prevent bubble coalescence and maintain small bubble size throughout the equipment. The froth containing the mineral particles usually overflows into a second vessel, where the froth is collapsed to recover the desired mineral. It is necessary to keep a relatively stagnant zone near the top of the flotation machine to prevent recirculation of the "loaded" bubbles to reduce the disengagement of particles from bubbles. Flint (1973) has reported that it is a usual practice to keep a constant depth of the froth separation zone on the scale-up. In flotation, gas-inducing impellers are primarily used to eliminate the difficulties associated with the use of spargers. The solid loading in the vessel can be as high as 40−60%. To capture the solid particles selectively, the impeller has to suspend the solid particles and bring about gas−solid contact. Considering all these aspects, the flotation cell should have the following characteristics: (i) the impeller should disperse the gas in the form of fine bubbles; (ii) the impeller should generate sufficient flow and turbulence to disperse the bubbles radially away from the impeller; (iii) it should suspend at least a part of the solids and to bring about bubble−particle contact; (iv) a stagnant zone should be present above the gas-inducing impeller, to allow the "loaded" bubbles to rise vertically upward; (v) a froth layer should be present near the top, which can then overflow into a separate vessel; (vi) there should not be intense backmixing in the liquid and recirculation of "loaded" bubbles should be avoided.

The use of gas-inducing impellers for gas−liquid contacting in the chemical process industry is gaining importance. In typical hydrogenation/oxidation applications, the heats of reaction are fairly large and the overall operation may be heat-transfer-controlled. In reactions where selectivity is of importance (ethoxylation, alkylation) it may be necessary to maintain uniform concentrations in the reactor; in such cases mixing is of prime importance. If the gas phase is sparingly soluble, the dissolved concentration of the gas is fairly small, and the overall reaction may become mass-transfer-controlled. From this discussion, it is clear that the important design parameters in gas−liquid−solid contacting are the fractional gas holdup, mass-transfer coefficient, critical impeller speed for the solid suspension, heat-transfer coefficient, mixing, and so forth. Over and above these characteristics, power consumption is important because it contributes significantly to the operating costs.

A preliminary literature survey has indicated several shortfalls of the existing literature. These are the following: (i) most of the investigations have been carried out in small-sized vessels (less than 0.5-m diameter) and over a limited range of operating conditions. The data from such experiments cannot be scaled up with confidence. (ii) Most of the investigations have been focused on a single design of the gas-inducing impeller, and a single-design objective like the rate of gas induction, mass-transfer coefficient, and so forth. (iii) There is no information in the literature on the design aspects of reactors employing gas-inducing impellers. To overcome some of these drawbacks, it was thought desirable to thoroughly analyze the reported literature. In this review, the reported designs of gas-inducing impellers are first classified. Extensive discussion has been given about the characteristic features of various designs reported in the literature. The hydrodynamic characteristics like the critical impeller speed for gas induction (N_{CG}), the gas induction rate (Q_G), and fractional gas holdup (ϵ_G), and so forth: and the performance characteristics such as the mass-transfer coefficients (k_La), solid suspension, and so forth are examined in detail. The purpose of this examination is to recommend a suitable geometry and identify correlations that can be used with a certain degree of confidence for scale−up purposes. A process design algorithm (stepwise procedure) is then presented for the design of reactors employing gas-inducing impellers. The algorithm involves the determination of the rate-controlling step, selection of equipment geometry and operating conditions, and an economic analysis to chose the optimum design. It is important to mention here that the above procedure does not rely on common scale-up rules such as geometric similarity, kinematic similarity, constant power consumption per unit mass, and so forth. The final selection of the equipment size and the geometry depends solely on economic considerations (which is the usual objective of process design engineers).

2. Classification of Gas-Inducing Impellers

Before starting a discussion on the various designs of gas-inducing impellers and their characteristics, it is useful to compare the characteristics of gas-inducing impellers with the other commonly used equipment like stirred tank reactors, bubble columns, packed columns, and so forth. Doraiswamy and Sharma (1984) and Kastanek et al. (1993) have given a detailed description of the characteristics of some of the equipment listed above. These are briefly summarized in Table 1A.

Packed columns and trickle-bed reactors give a very low-pressure drop and they can handle large quantities of gas. However, these reactors have poor heat-transfer characteristics and are also unsuitable as dead end systems. Also, these pieces of equipment do not provide flexibility with respect to liquid-phase residence time and are not suitable when the liquid-phase reactions are slow.

Stirred tank reactors have good heat- and mass-transfer characteristics. The ability to suspend solid particles is also very good. For these reasons stirred vessels have become very popular in the chemical industry. However, they have a low gas-handling capacity. For the recycle of unreacted gas an external recycle gas compressor has to be employed which may make the overall operation economically unattractive.

Bubble columns/air lift loop reactors also have good heat- and mass-transfer characteristics. The gas-

Table 1.

A. Characteristics of Different Types of Reactors

	packed column/ trickle-bed reactors	stirred-tank reactors	bubble column/ air lift loop reactors	gas-inducing contactors
gas-phase pressure drop	low	low	moderate	low−moderate
gas handling capacity	high	low−moderate	moderate	low−moderate
gas-phase residence time distribution	plug flow	back-mixed	back-mixed	back-mixed
liquid-phase residence time	low	moderate−high	moderate−high	moderate−high
mass-transfer characteristics	poor	good	good	good
heat-transfer characteristics	poor	good	good	good
solid/catalyst suspension	packings can be made to act as catalyst	good	external loop has to be provided to induce gross liquid circulation	good (solid suspension in PJR needs to be investigated)
unreacted gas recycle/pure gas	requires external recycle gas compressor	requires external recycle gas compressor	requires external recycle gas compressor	internal; does not require external recycle gas compressor

B. Comparison of Different Types of Systems

	type		
feature	11	12	22
standpipe	not required	not required	necessary
stator	not required	optional	optional
impeller hood	not required	optional	beneficial
hollow impeller	necessary	necessary	not required
impeller shroud	not required	necessary	optional
liquid feed to impeller zone	irrelevant	optional	optional
liquid feed to standpipe	irrelevant	irrelevant	optional
example	hollow pipe impeller	outoukumpu flotation cell	turboaerator

handling capacity is high but the gas-phase pressure drop is high. For achieving solid suspension, an external loop has to be provided to generate gross liquid circulation. Again, the recycle of unreacted gas can be made possible only with an external recycle gas compressor. These types of reactors may be economically attractive at large capacities.

Gas-inducing contactors have good heat- and mass-transfer characteristics. Solid suspension can also be achieved. However, the major advantage of such a system is that it can recycle the gas internally. A dead end system can be used most effectively for systems involving pure gases. A dead end system can induce gas from the headspace and thus eliminates the need for spargers or porous plates.

The gas-inducing impeller plays a key role in the gas-induction process. It induces the gas from the headspace and creates a gas−liquid dispersion. It also generates a liquid flow for the dispersion of the induced gas. Therefore, Mundale (1993) has classified the gas-inducing impellers, on the basis of the flow pattern in the impeller zone. The gas enters the impeller zone at one location and leaves at another location. Along with the gas, the liquid can also enter the impeller zone and leave along with the gas. The nature of the flow entering and leaving the impeller zone is used as the criterion to classify the impellers: (i) Single-phase flow (gas alone) at the inlet as well as at the outlet of the impeller zone (type 11 system) (ii) Single-phase flow (gas alone) at the inlet and two-phase flow (gas and liquid) at the outlet of the impeller zone (type 12 system). (iii) Two-phase flow (gas and liquid) at the inlet as well as at the outlet of the impeller zone (type 22 system).

The above three types of gas-inducing impellers are depicted in Figure 1. Table 1B summarizes the essential features of each type of system. In general, type 12 and 22 systems involve gas−liquid two-phase flow, and hence these systems are less amenable to theoretical analysis with the present status of knowledge. Type 11 systems are relatively easy to analyze on the basis of the fundamental principles, as they involve only single-phase gas flow. It is interesting to note that the

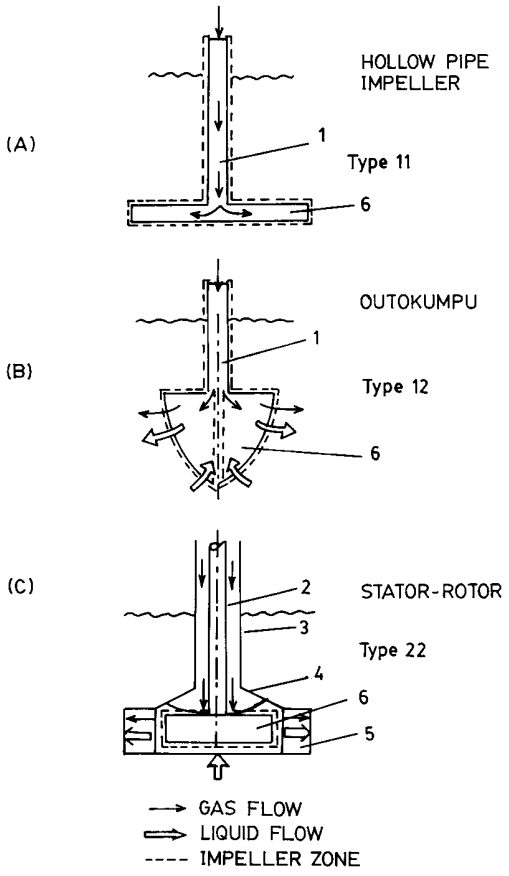

Figure 1. Three types of gas-inducing impeller designs. (1) Hollow shaft; (2) solid shaft; (3) standpipe; (4) stator; (5) stator vanes; (6) impeller.

wide variety of gas-inducing impellers as well as flotation machines reported in the literature can be completely classified in the above manner.

2.1. Type 11 Systems. The simplest kind of type 11 system is a cylindrical, hollow pipe with an orifice (Figure 2A). These are collectively called hollow pipe

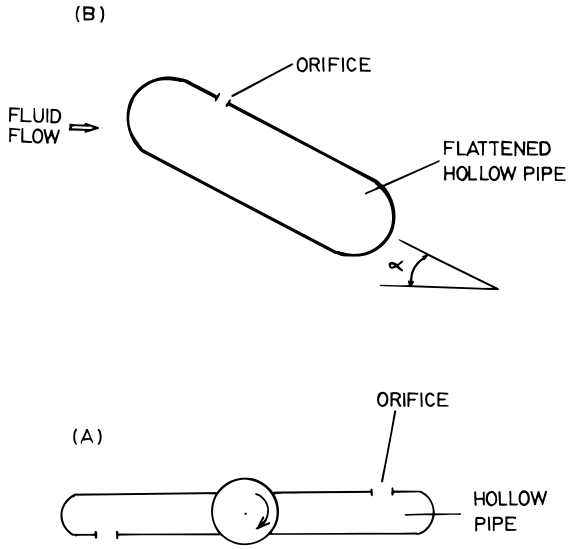

Figure 2. Hollow pipe gas-inducing impeller (courtesy, Martin, 1972): (A) Schematic representation; (B) flattened hollow pipe impeller at an angle of attack, α.

impellers. The hollow pipe is mounted on a hollow shaft. This type of configuration has been studied extensively [Zlokarnik and Judat (1967), Martin (1972), Topiwala and Hamer (1974), Joshi and Sharma (1977), Joshi (1980), Baczkiewicz and Michalski (1988), Evans et al. (1990, 1991), Rielly et al. (1992), Forrester and Rielly (1994), Forrester et al. (1994), Heim et al. (1995)]. When this impeller rotates in a vessel, a pressure reduction occurs at the orifice per Bernoulli's equation. When the reduction in local pressure is sufficient to overcome the hydrostatic head of the liquid, gas induction occurs.

Martin (1972) has measured the values of the pressure differential generated for hollow pipe impellers at different locations of the orifice. The orifice angle was measured from the front stagnation point. He has reported that, for a given impeller speed, the extent of pressure reduction is maximum for an orifice angle of 80°. He has also measured the rate of gas induction for different orifice locations. It was observed that the rate of gas induction is maximum when the orifice angle was 105°, when compared on the basis of the pressure differential generated. This difference between the location of the maximum pressure differential and maximum rate of gas induction was attributed to the difference in the pressure profiles in the presence of gas bubbles. He has proposed that the swarm of bubbles rising upward generates an upward current of water, which modifies the pressure field in the vicinity of the orifice.

Another interesting effect is that the rotation of the impeller causes flow separation at the downstream side of the cylinder, forming a wake region. This causes the formation of a gas cavity and a reduction in the average density in the immediate vicinity of the impeller. This leads to a reduction in the power consumption, and correspondingly the local pressure profile gets modified. To prevent a reduction in the pressure differential, the flow separation has to be prevented.

The studies on type 11 impellers can be considered to have been carried out with the following objectives: (i) Maximizing the pressure differential generated for a given impeller speed (This was achieved by varying the number of pipes and the shape, number, and angle of attack, and so forth.); (ii) locating the orifice in the region of lowest local pressure so that the driving force for the gas induction is maximum (Changing the orifice location, both on and off the blades, was used to achieve this. Keeping in mind Martin's (1972) study, it can be clearly seen that the location of the maximum pressure differential need not be the location of the highest gas-induction rate.); (iii) minimizing the pressure drop associated with the gas flow rate, so that the per unit driving force, larger amount of gas can be induced. (This can be achieved by varying the size and number of orifices.). A number of efforts have been made to achieve these different objectives and have resulted into various designs of hollow pipe impellers.

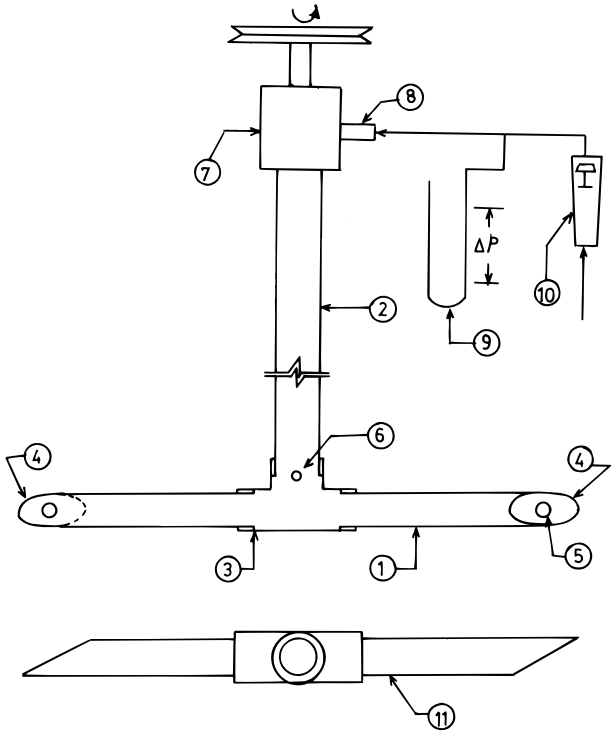

Figure 3. Modification to the hollow pipe impeller design (courtesy, Joshi, 1980): (1) hollow tube; (2) hollow shaft; (3) hub; (4) 45° cut at the impeller tip; (5) hole through which gas induction occurs; (6) hole drilled on hub; (7) seal; (8) gas inlet; (9) manometer; (10) rotameter; (11) plan view of the impeller.

Zlokarnik and Judat (1967) have investigated hollow pipe and disk stirrers which can be considered as a large number of hollow pipes. Martin (1972) created an aerofoil shape by flattening the cylindrical impeller and changing the angle of attack of the impeller (Figure 2B). This was done to prevent the flow separation behind the blades. This improvement lead to a 50−100% increase in the gas-induction rate.

Joshi and Sharma have (1977) varied the total orifice area by a factor of 200, by changing the orifice diameter as well as the number of orifices, which gave a similar increase in the gas-induction rate. Joshi (1980) has used a hollow cylindrical impeller but with small holes drilled on the hub of the impeller (Figure 3). When such impeller rotates, a stream of liquid enters through the holes on the hub and comes out through the orifice along with the gas. Such a liquid stream was visually observed, and it helped in breaking up the gas cavity. The driving force for this liquid stream is the pressure

Table 2. Comparison of Different Types of Impellers Studied and the Range of Investigation

name	type	operating parameters	refs
pipe impeller	11	$T = 28$ cm, $D = 25$ cm, $D_P = 1.25$ cm, $N = 3-6$ rps, $S = 20$ cm, $C = 10$ cm, flattened cylindrical 0.86×1.48 cm, angle of attack $= 0-15°$	Martin (1972)
hollow pipe	11	$T = 0.158$ m, $D = 0.075$ m, $C = 0.059$ m, $S = 0.10$ m, $N = 12-25$ rps, hollow pipe impeller	Topiwala and Hamer (1974)
conical impeller	12	$T = 0.29$ m, $D = 0.045-0.075$ m, $S/D = 2-4$, $N = 40-100$ rps, impeller consists of two cones with bases touching, conical disperser	Koen and Pinguad (1977)
Denver, Wemco cells, turboaerator	22	$T = 0.1-0.3$ m square, $D = 0.07-0.115$ m, $S/T = 0.3-0.9$, water and polyethylene glycol,	Sawant and Joshi (1979)
turbo aerator	22	$T = 40$ cm, $D = 8-12$ cm, $d/D = 0.5$ and 0.67, $D_S/D = 1.4$ and 1.25, $S = 0.5-2.0$ m, $N = 16-40$ rps, stator blade angle 30°	Zundelevich (1979)
pipe, modified pipe	11	$T = 41-100$ cm, $D = 20-50$ cm, $D_P = 2.5-3.2$ cm, no. of pipes $= 2-6$, $W = 3.2-5$ cm, $S = 0.3-0.9$ m, $N = 2-12$ rps	Joshi and Sharma (1977), Joshi (1980)
Wemco cell type impeller	22	$T = 30$ cm, $D = 10$ cm, $S = 7-15$ cm, $N = 5-30$ rps	Sawant et al. (1980)
Denver cell type impeller	22	$T = 14 \times 14$ to 38×38 cm, $D = 7-20.4$ cm, $S/T = 0.2-1.0$, $N = 5-19$ rps	Sawant et al. (1981)
multiple impeller system	22	$T = 0.19-0.316$, $D/T = 0.25$ m, propeller near-surface and axial turbine near-bottom mounted on different shafts, $N = 0-15$ rps, water, sodium alginate, tween 20 surfactant	Matsumura et al. (1982a−c)
helical screw in draft tube	22	report based on 2.5 L, followed by 150-L and 3900-L test reactor	Litz (1985)
PBTD with stator	22	$T = 57$ cm, $C/T = 0.33$, $S/T = 0.5-1.25$ $D = 15-25$ cm, $N = 3-14$ rps	Raidoo et al. (1987)
pipe impeller	11	$T = 44$ cm, $D = 15.4-24.2$ cm, $D_P = 0.6$ cm, $C = 6.6$ cm, $S = 60$ cm, $N = 6.4-23$ rps	Baczkiewicz and Michalksi (1988)
pipe impeller	11	$T = 29$ cm, $D = 13$ and 22.5 cm, orifice locations 2.5−5.5 cm from shaft, $C = 0.1$ m, $S = 0.05-0.30$ m, $N = 0-8$ rps	Evans et al. (1990, 1991)
hollow-bladed impeller	11	$T = 30-60$ cm, $D = 21.5$ cm, orifice locations 7.5 cm from shaft axis, paddle, and concave-bladed impeller, $S = 0.05-0.55$ m, $N = 1-9$ rps	Rielly et al. (1992)
PBTD with stator	22	$T = 57-150$ cm, $D = 19-50$ cm, $W = 4-10$ cm, $D_S = 226-270$ cm, blade angle 30−90°, no. of blades 4−12, $S = 0.2-1.2$ m, $N = 2-14$ rps	Mundale (1993)
standpipe and rotor	22	$T = 0.77-15.2$ cm^2 cylindrical, $D = 0.16-0.41$ m, with and without vortex enhancer	Brenner et al. (1994)
pipe and turbine impellers	11 and 12	$D = 5-6.5$ cm, $D_S = 7.4-9.4$ cm, $V = 6$ l, $T = 0.20$ m, $N = 0-25$ rps, water, salt solution, and sucrose solution	Aldrich and van Deventer (1994)
hollow-bladed	11	$T = 0.45$ m, $D = 0.154$ m, $C = 0.225$ m, $S = 0.225$ m, $N = 4-10$ rps, sparging rate $= 0-400$ cm^3/s, concave-bladed, multiple-orifice impellers	Forrester et al. (1994), Forrester and Rielly (1994)
hollow-bladed impeller	11	$T = 60$ cm square, $D = 21.5$ cm, $C = 16.8$ cm, $S = 8-40$ cm, $N = 2-10$-rps orifice locations 7.65 cm from shaft axis, two-bladed disc turbine	Rigby et al. (1994)
Denver	22	$T = 0.19$-m square, $D = 0.096$ m, $D_S = 0.127$ m, $C = 1.5$ cm, 0−100 ppm PGME additive $S = 0.22$ m, $N = 10-25$ rps	Al Taweel and Cheng (1995)
hollow pipe	11	$T = 0.3$ m, $D = 0.1-0.15$ m, 4 and 6 hollow-bladed, disk impeller $C = 6.5$ cm, $S = 0.9-2.9$ m, $N = 6-12$ rps	Heim et al. (1995)
shrouded turbine	22	$T = 0.19$ m, $D = 0.05$, 0.06 m, shroud consists of a slotted draft tube, $N = 0-25$ rps, temp $= 8-80$ °C water, sucrose solution, isopropanol	Aldrich and van Deventer (1996)
PBTD with stator	22	$T = 0.57-1.5$ m, $D = 0.19-0.5$ m, $C = 0.09-0.5$ m, $S = 0.1-0.6$ m, $N = 2-10$ rps, single- and multiple-impeller system, different designs of bottom impeller	Saravanan and Joshi (1995, 1996), Saravanann et al. (1996, 1997)
PBTD with stator	22	$T = 1.5$ m, $D = 0.5$ m, $C = 0.8$ m, $S = 0-0.4$ m, $N = 1-4$ rps. multiple-impeller and sparger system, different designs of bottom impeller, $V_G = 0-29$ mm/s	Patwardhan and Joshi (1997)

differential between the orifice located on the blade and the hole drilled on the hub. The orifice on the impeller blade has a velocity equal to the impeller tip velocity. The impeller tip velocity is equal to $\omega D/2$. Since the hub radius is much smaller than the impeller radius, the hole drilled on the hub has only a fraction of the tip velocity. This results in a substantial pressure difference between the two, resulting in a jet of liquid stream entering from the hub and leaving the tip. This resulted in a 20−30% increase in the gas-induction rate. Baczkiewicz and Michalski (1988) have also used hollow pipe impellers. The pipe was designed in such a way that the downstream side of the pipe was cut away completely. This amounts to having an infinite number of orifices on the pipe. However, they have not compared the performance of their system with other designs of hollow pipe impellers.

Rielly et al. (1992) and Forrester et al. (1994) have investigated hollow, concave-bladed impellers. The curvature of the blades in the downstream side was intended to reduce the flow separation. The blades in such a type of impellers were mounted on a disk and connected to a hollow shaft through which the gas induction occurs. Rigby et al. (1994) located the orifice not on the blade but slightly off it. The distance of the orifice from the blade surface was varied to achieve the maximum gas-induction rate. The increase in the rate of gas induction was found to be 10−15%. Forrester and Rielly (1994) used multiple orifices on the blades to improve the gas-induction characteristics. By increasing the number of orifices, they effectively increased the area through which gas induction begins, without increasing the bubble size. Heim et al. (1995) have used four- and six-pipe impellers. As the number of hollow

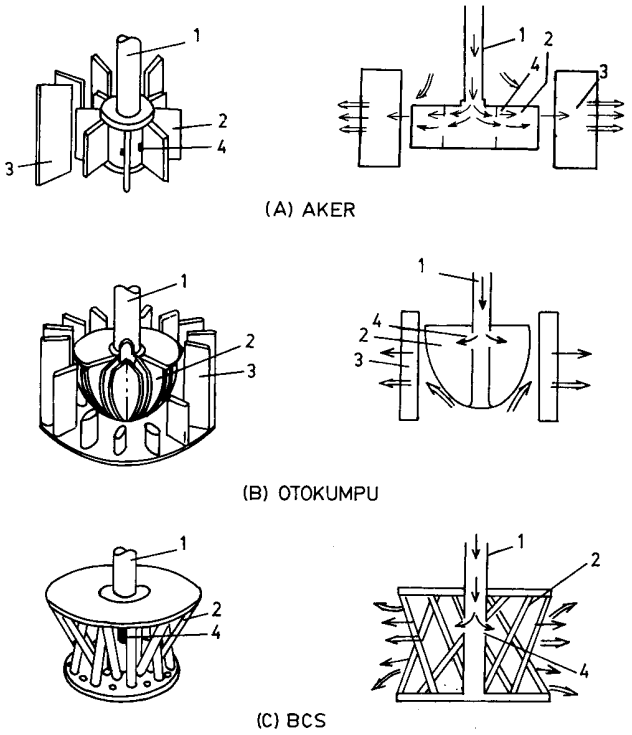

Figure 4. Different designs of type 12 flotation cells (reproduced from Barbery, 1984): (A) Aker; (B) Outokumpu; (C) BCS. (1) Hollow pipe; (2) impeller; (3) stator/disperser vanes; (4) orifice for air delivery into impeller zone.

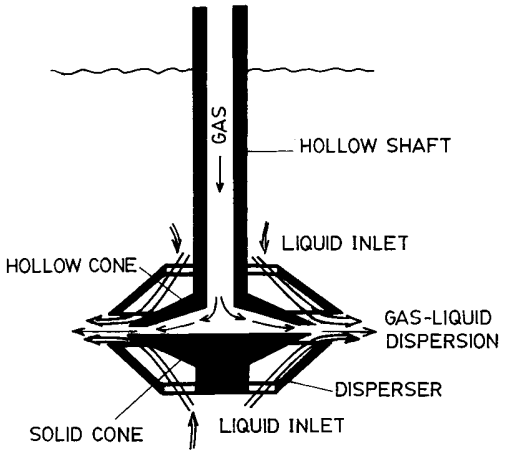

Figure 5. Rotating disperser system (courtesy, Koen and Pingaud, 1977).

pipes increases, their design approaches that of a disk impeller. They have shown that such a disk impeller is superior to four- or six-pipe impellers. Table 2 summarizes the range of different variables covered in these studies.

2.2. Type 12 Systems. A large number of flotation machines fall in this category, for example, Aker (Barbery (1984), Figure 4A), Outokumpu (Fallenius (1981), Figure 4B), and BCS (Barbery (1984), Figure 4C). The characteristic feature of this type is that the gas is delivered into the impeller region via a hollow shaft through an orifice or an air port and the gas−liquid dispersion leaves the impeller region via a stator, a diffusor, or an impeller shroud. The rotating disperser system (Figure 5) reported by Koen and Pingaud (1977) and the double-finger impeller reported by Schubert and Bischofberger (1978) also fall in this category. The

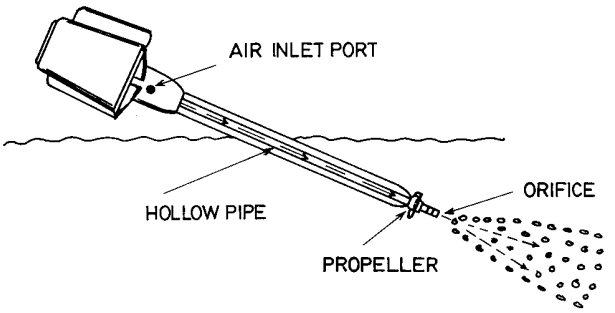

Figure 6. AIRE−O_2 system (courtesy, Aeration Industries International Inc., U.S.).

AIRE−O_2 system developed by the Aeration Industries International, Inc. (U.S.) (Figure 6) and EOLO$_2$ system developed by Acqua and Co. (Italy) (Figure 7) also belong to this type.

The essential features of a type 12 system include a hollow shaft, an impeller, orifices/air ports, and a stator/diffuser. The impeller rotation causes a reduction in the local pressure. At sufficiently high impeller speeds, air is drawn in through the hollow shaft and gets introduced in the impeller zone through orifices or air ports located near the impeller on the hollow shaft. Along with the induced air, extra air may be blown through the hollow shaft, depending on the requirement of the specific application. The impeller also helps in generating liquid-phase flow for the dispersion of induced gas. The stator/diffuser helps to generate high shear in the impeller zone to create finer bubbles. The variation between the various designs is mainly in the geometry of these various parts which depend on the manufacturer.

The Aker design consists of an impeller and a diffuser system. The impeller hub has air ports which induce the gas into the liquid. The induced gas gets dispersed in the form of bubbles because of the shear caused between the impeller and the diffuser blades. The blades of this type of impeller resemble those of a straight blade turbine. The diffuser system consists of blades (or vanes) that surround the impeller. The diffuser blades can be set at an angle to the radius vector. The impeller rotation causes mainly tangential flow in the region between the impeller and the diffuser. This flow impinges on the diffuser blades and gets deflected. The overall flow pattern leaving the impeller−diffuser region therefore becomes radial. In this manner the diffuser guides the flow out of the impeller zone and improves the dispersion characteristics.

The Outokumpu design is similar to the Aker design but the impeller is hemispherical in shape. The BCS design consists of a hollow shaft with an air port. The impeller of this design consists of an assembly of rods held between two disks. There are two sets of rods, one set is inclined radially inward and the other set is inclined radially outward. The two sets alternate each other, causing the flow generated by one to impinge on the other. This causes a reduction in the bubble size and improves the dispersion characteristics.

The rotating disperser system of Koen and Pingaud (1977) consists of a hollow shaft connected to the impeller. The dispersing device consists of two coaxially mounted cones. The top and the bottom cones have a hole at the center that allows an ingress of the liquid from the top as well as the bottom. The two cones are slightly separated forming a disk-shaped space between

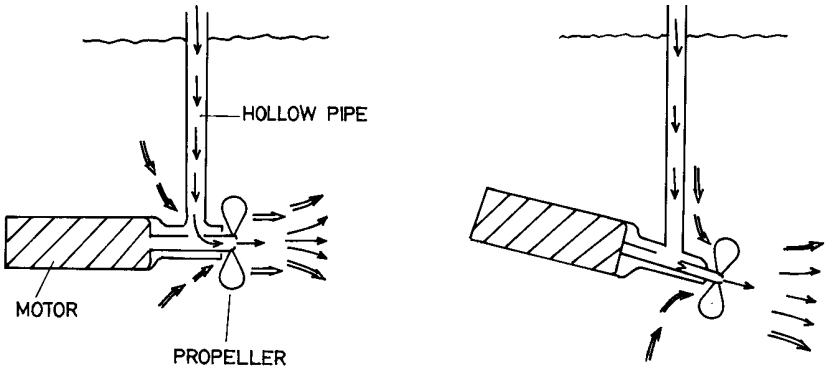

Figure 7. $EOLO_2$ system (courtesy, Acqua and Co., Italy).

them. The impeller itself consists of two cones mounted with their bases touching. A gas−liquid dispersion flows radially outward from this disk-shaped space into the bulk of the liquid. They have further claimed that this impeller can also be used for liquid−liquid systems.

The AIRE−O_2 system consists of a propeller mounted on a hollow shaft. The motor driving the propeller is located above the surface of the water. The propeller forces the water to flow past the end of the shaft at a high velocity. The high local velocity causes a reduction in the local pressure per Bernoulli's equation, thus drawing air from the atmosphere through the hollow shaft. The literature reports that the oxygen utilization efficiency (oxygen uptake for every unit of oxygen delivered into the water) of such a system is about 16−18% as compared to a diffuser aeration efficiency of 8−10% and a surface aeration efficiency of 10−12%. The mixing time for a 1-acre pond with a single 2 hp. AIRE−O_2 system is reported to be 32 min. Additional features of the system are lightweightness, the ability to position the system at any angle to the vertical, the ease of installation, and the ability to operate even when the temperatures are below freezing. The $EOLO_2$ system is similar in construction. The main difference is that the entire motor can be kept below the surface of water up to a depth of 15 m. Like the AIRE−O_2 system, it is easy to install and lightweight and can be rotated to position at any angle with the vertical. Such a flexibility gives a wide choice of flow patterns. A direct comparison of these commercial designs with those reported in the literature is not possible, because of the lack of scientific information on the commercial designs. Data on the gas-induction rate (Q_G), fractional gas holdup, mass-transfer coefficient, mixing time, solid suspension ability, and so forth as a function of the power consumption (P_G) would have been very useful in comparing the AIRE−O_2 and $EOLO_2$ systems with other systems.

2.3. Type 22 Systems. A large variety of type 22 systems exist. These include the flotation cells as well as rotor−stator systems. Some of the main designs are Wemco (Degner and Treweek (1976), Figure 8A), Wedag (Arbiter and Steininger (1965), Figure 8B), Denver (Taggart (1960), Figure 8C), Agitair (Arbiter and Steininger (1965), Figure 8D), Booth (Barbery (1984), Figure 8E), Sala (Harris (1976), Figure 8F) flotation cells, turboaerator (Zundelevich (1979), Figure 9), pitched turbine impellers covered with a stator−standpipe assembly (Raidoo et al. (1987), Mundale (1993), Saravanan et al. (1994)), and multiple-impeller systems (Saravanan and Joshi, 1995). The characteristic features of these systems include a (i) rotor/impeller, (ii) standpipe through which the gas induction takes place, and (iii) stator/diffuser surrounding the impeller.

The basic principle of operation of the stator−standpipe system is as follows. The rotation of the impeller causes a vortex formation in the standpipe. As the impeller speed increases, the vortex depth progressively increases. When the vortex is sufficiently near the impeller, the impeller blades shear the gas−liquid interface, entrapping gas bubbles. The entrapped gas bubbles are then carried away by the flow generated by the impeller. The rotation of the impeller also causes a reduction in the local pressure per Bernoulli's equation. This would lead to an ingress of the liquid from the region outside the stator. The stator consists of an impeller hood, vanes, and an air ring. The vanes, vane shrouding ring, and the vane air ring are collectively referred to as a diffuser. The impeller hood prevents the entry of liquid into the impeller zone from above. The air ring prevents the axial downward flow from the impeller. As a result of the impeller hood and the air ring, the liquid flow coming out of the stator is radial. The stator vanes can be set at an angle to the radius vector. The entire diffuser zone resembles the diffuser of a centrifugal pump. The radial flow of fluid leaving the impeller enters the diffuser zone. The fluid then flows through a region formed between two stator vanes. Since the stator vanes are set at an angle, the cross sectional area gradually increases, and as a result, the velocity gradually decreases. This results in pressure recovery to some extent, and the fluid leaves the diffuser with reduced shock as compared to that in the absence of a diffuser.

Wemco, Denver, Booth, and Wedag flotation machines have all these characteristic features. All the designs have some additional features, which vary depending on the manufacturer. These flotation machines have not been developed in an evolutionary manner, but are rather empirical in nature. The rotor of the Wemco design consists of cylindrical rods called posts mounted between two disks. The diffuser and the impeller hood for this design consists of a conical perforated plate. The gas−liquid dispersion is forced out through these perforations. This system was investigated by Sawant et al. (1980).

The impeller of the Denver-type machines is disk-shaped with blades mounted on the edge of the disk. The stator consists of vanes that are fixed to the stator hood. There is no air ring in this type of design. Outside the standpipe, there is a conical section called the recirculation well. Liquid can enter through the top of this well. Because of the conical shape, the liquid effectively gets injected into the impeller region. An air

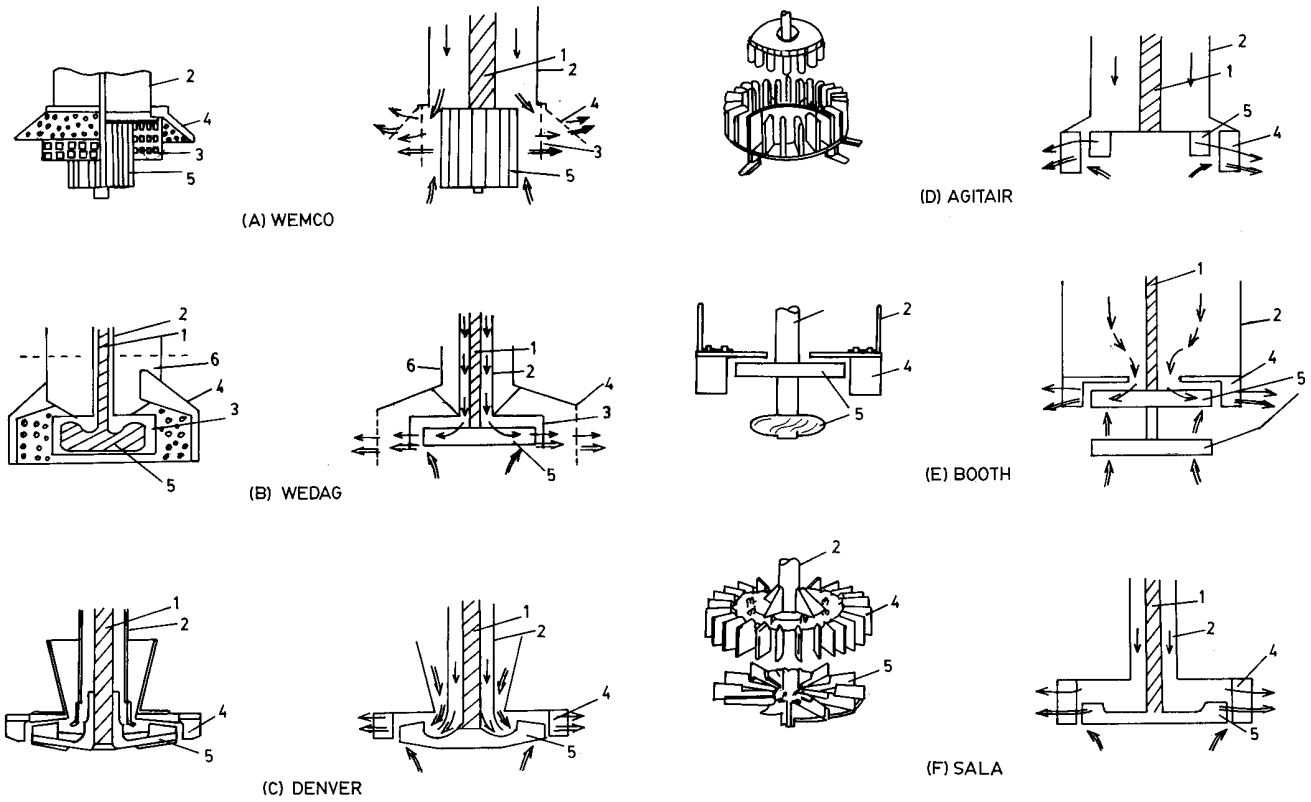

Figure 8. Different designs of type 22 flotation cells (reproduced from Barbery, 1984): (A) Wemco; (B) Wedag; (C) Denver; (D) Agitair; (E) Booth; (F) Sala: (1) (solid shaft; (2) standpipe; (3) stator/disperser; (4) disperser hood.

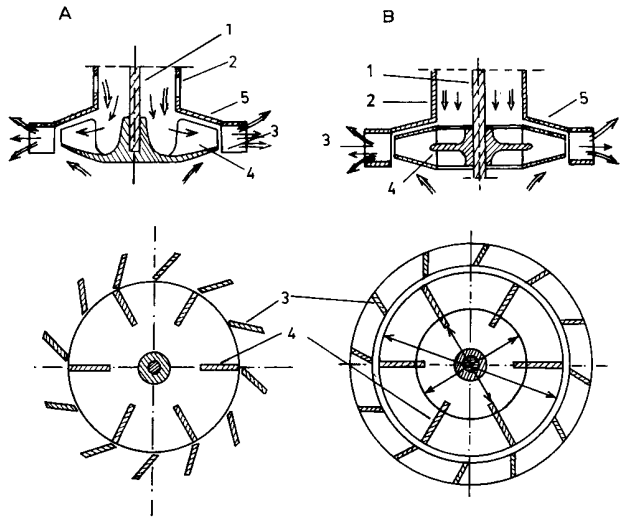

Figure 9. Turboaerator designs (courtesy, Zundelevich, 1979): (1) solid shaft; (2) standpipe; (3) stator vanes; (4) impeller; (5) stator hood.

belt is a conical attachment at the bottom of the standpipe. Its function is to direct the induced air onto the impeller blades and to prevent the direct entry of gas bubbles through the recirculation well. The Denver cell was investigated by Sawant et al. (1981).

The Agitair impeller consists of a disk on which the cylindrical rods called fingers are mounted. The disk on which the impeller fingers are mounted has an annular space for pulp recycle into the impeller region. This means that both gas and liquid can enter the impeller region; the gas−liquid dispersion created in the impeller region is then distributed with the help of a diffuser.

Matsumura et al. (1982a−c) have investigated a multiple-impeller system. In their work, the two impellers are driven independently, so that their speeds could be adjusted independent of each other. In their system the upper impeller is a propeller. This impeller is located close to the liquid surface and rotates at high speeds. It generates turbulence at the liquid surface and is able to produce a large number of fine bubbles. The second impeller which is an axial flow type is located near the base of the tank. This impeller creates gross liquid circulation for the uniform dispersion of the bubbles generated. A draft tube is installed on the free liquid surface to prevent accumulation of the froth which reduces the gas-induction capacity. Matsumura et al. (1982c) have used the rector as a fermenter using pure oxygen. They have investigated the performance of the fermenter in terms of the biomass productivity, energy requirement, and oxygen utilization efficiency.

Litz (1984, 1985) has employed a helical screw in a draft tube as a gas-inducing impeller. Figure 10 shows a schematic of their reactor. A baffle arrangement provided at the top of the draft tube generates a number of vortices from which gas induction takes place. When the helical screw impeller rotates, an axially downward liquid flow is generated. Because of this liquid flow, the entrapped gas bubbles are carried downward through the draft tube. At the bottom of the draft tube these bubbles rise vertically, a circulation pattern is established, and good gas dispersion is achieved in the rector. Litz (1985) has given certain performance characteristics of such reactors. The relative power draw (ratio of power consumption under gassed and ungassed conditions) is almost 1.0 up to a gas holdup of 10%. It was also shown that when such a reactor was employed for a oxyhydrolysis reaction, the residence time can be

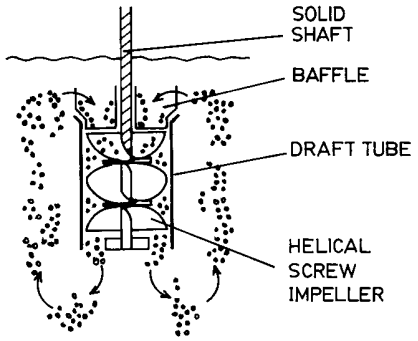

Figure 10. Helical screw impeller in a draft tube (courtesy, Roby and Kingsley, 1996).

reduced by approximately 40% as compared to that of conventional stirred tank reactors. As a result, the power consumption reduces by 25%.

Litz et al. (1990), Kingsley et al. (1994), and Roby and Kingsley (1996) have made further modifications to this reactor. These modifications consist of providing a gas-containment baffle, a sparger, a compound impeller design, and so forth. The helical screw inside the draft tube, or a conventional agitator, generates a liquid flow necessary for the dispersion of the sparged gas. The gas-containment baffle separates the vessel into two zones and it helps to keep the gas bubbles in circulation in the reactor. The gas-containment baffle is particularly useful for reactions employing pure oxygen. It helps to keep the partial pressure of oxygen in the rector headspace below the flammable limit and ensures hazard-free operation.

The Booth design does not have a stator air ring. However, below the gas-inducing impeller, a second impeller, typically a propeller, is provided to improve the gas dispersion. This is one of the earliest reported uses of a multiple-impeller system. Saravanan and Joshi (1995, 1996) and Saravanan et al. (1996, 1997) have carried out extensive investigations on the multiple-impeller system. Both the impellers were located on the same shaft, and hence they have to be operated at the same speed. They have reported that when a single gas-inducing impeller is located close to the top liquid surface for maintaining a high rate of gas induction, it suffers from several drawbacks. These include poor dispersion of the induced gas, poor solid suspension ability, and so forth. These arise from the fact that the liquid flow and turbulence characteristics are feeble in a major portion below the gas-inducing impeller. These drawbacks were observed to be more serious with an increase in the scale of operation. These limitations of the single-impeller system have overcome by using a second impeller below the gas-inducing impeller. The gas-inducing impeller can then be kept close to the top liquid surface (about 100−200 mm below the liquid surface), irrespective of the scale of operation, to ensure a high gas-induction rate. For other duties like gas dispersion (distribution of the induced gas throughout the equipment), solid suspension, heat transfer, mixing, and so forth to be performed, the second impeller was used. The design of the lower impeller was further optimized for different duties such as gas holdup, solid suspension ability, and so forth. This activity has clearly shown that the optimum design of the lower impeller changes with the design objective. For example, to achieve high fractional gas holdup, it was desirable to use an upflow impeller at the bottom, whereas to achieve good solid suspension, a downflow impeller at the bottom was desirable.

Aldrich and van Deventer (1994) have investigated the effect of solid particles on the rate of gas induction from turbine impellers. Brenner et al. (1994) have used a turboaerator along with a standpipe. The characteristic feature of their system is that the standpipe was fitted with radial fins which enhance the vortices formed near the impeller and as a result increase the gas-induction rate.

Hsu and Chang (1995), Hsu and Huang (1996, 1997), and Hsu et al. (1997) have described a different configuration. The system consists of an unbaffled tank fitted with one or two impellers. Since the tank is unbaffled, a vortex is generated in the tank, whose depth progressively increases with the impeller speed. At a certain speed the vortex reaches the impeller and is broken up into gas bubbles. This reactor can actually be described as a surface aerator. The gas phase in their investigations was the ozone in a dead end configuration. In much of their work, Hsu and Chang (1995), and Hsu and Huang (1996, 1997) report the ozone utilization efficiency as a function of various operating parameters. The data on ozone utilization efficiency are not at all useful for the design of a reactor for any other application. Only recently (Hsu and Huang (1997)) have correlations been provided for power consumption, critical impeller speed for gas induction, and so forth. No correlation has been given for other important parameters such as the gas-induction rate, gas holdup, mass-transfer coefficient, and so forth. Moreover, their work is carried out on small-sized vessels (0.17-m diameter); hence, their results are not expected to be useful for scale-up.

Patwardhan and Joshi (1997) have employed a gas-inducing impeller in mechanically agitated contactors. They have also presented a rationale for the use of a gas-inducing impeller in MAC. Figure 11A shows a schematic of such a reactor. In such pieces of equipment, the gas sparged at the bottom gets dispersed throughout the vessel with the help of impellers. Unreacted gas escapes into the headspace. The gas-inducing impeller enables the recirculation of the unreacted gas from the headspace. The role of the gas-inducing impeller in such reactors is, at least, to recirculate the unreacted gas. If the gas-inducing impeller is able to induce gas at a rate greater than the unreacted gas rate, then a part of the gas−liquid contacting duty is performed by the gas-inducing impeller. If the amount of sparged gas still remains the same, then on a unit reactor volume basis more gas can be handled and higher productivity can be realized. The productivity in such reactors depends on the gas-induction rate (Q_G), the fractional gas holdup (ϵ_G), and so forth. Therefore, the design of the gas-inducing impeller plays an important role on the overall performance of the reactor. It is also important to note that, in such reactors, the type of sparger, the rate of sparging, and so forth. affect the performance of the gas-inducing impeller itself. Thus, the overall performance of such reactors involves an interplay of the sparged gas and the induced gas. An optimum design of such reactors therefore involves striking a fine balance between the rate at which gas can be sparged, the sparger design, the gas-inducing impeller design, the rate of gas induction, and so forth. Patwardhan and Joshi (1997) have investigated the effects of the sparger

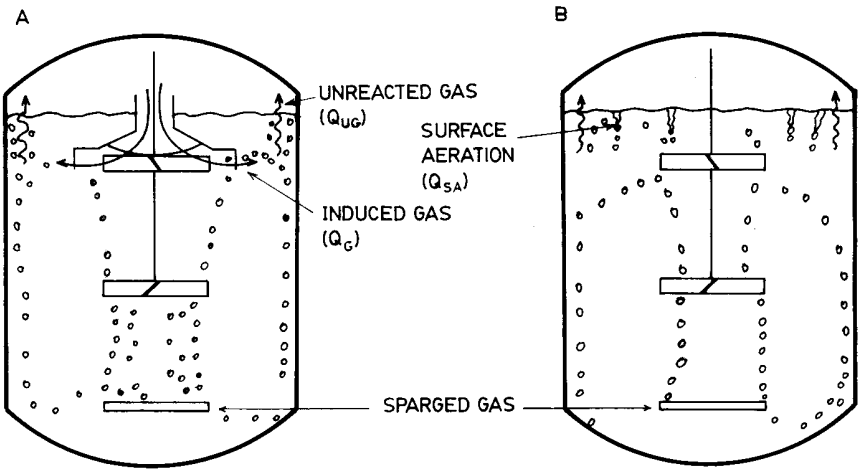

Figure 11. (A) Schematic representation of GIC equipped with a gas-inducing impeller and a sparger; (B) schematic representation of MAC without a gas inducing impeller.

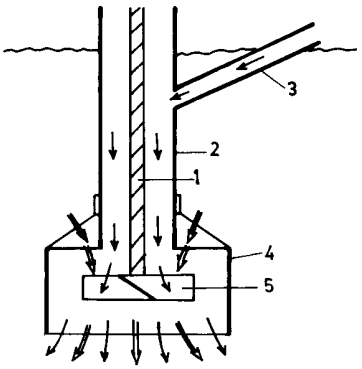

Figure 12. TDS-induction mixer (courtesy, Yastral GMBH).

size, lower impeller design, and the superficial velocity of the sparged gas on the gas-induction rate and the fractional gas holdup. In the absence of a gas-inducing impeller, the system resembles a conventional mechanically agitated contactor (MAC) and gas recycle takes place by surface aeration alone (Figure 11B).

The Yastral design (Yastral GMBH) can also be considered as a stator−rotor system. This design (Figure 12) was shown to be very convenient for handling solids. The impeller is located in the vessel, and the standpipe is connected to a hose pipe. When the impeller rotates, suction is created which sucks the solids from a silo or a bag through the standpipe into the reaction vessel. In fact, all the type 22 designs can be conveniently used for the suction of solids.

3. Hydrodynamic Characteristics

3.1. Critical Impeller Speed for the Onset of Gas Induction. 3.1.1. Type 11 System. The hollow pipe impeller (type 11 system) induces gas through an orifice. The impeller rotation causes liquid velocity to increase. This causes a reduction in the pressure at the orifice outlet. At a particular impeller speed, the local pressure (according to Bernoulli's equation) becomes low enough to overcome the liquid head over the orifice and gas starts to induce into the liquid. This is called the critical impeller speed for gas induction and is denoted as N_{CG}. Thus, the critical speed is determined by a balance of pressure and velocity head. Neglecting, the frictional pressure losses, Bernoulli's equation can be written as

$$\mathrm{d}\left(\frac{\rho_L U^2}{2}\right) + \mathrm{d}P = 0 \tag{1}$$

Here, P is the combined hydrostatic and pressure head. To predict the critical impeller speed, the velocity and the pressure heads have to be related to the impeller speed. The velocity head is typically based on the impeller tip velocity (with or without slip). The relationship of the local pressure head with the impeller speed depends on many factors such as the impeller geometry, physicochemical properties of the liquid, shape of the blades, and so forth. If the local pressure is related to the impeller speed, then eq 1 can be used to estimate the critical impeller speed for the onset of gas induction. This section deals with the prediction of N_{CG} starting from eq 1.

Martin (1972) has used the theory of flow past immersed bodies. A cylindrical impeller rotating inside a liquid can be considered as if the impeller is stationary and the fluid outside is flowing past the cylinder. If the fluid is considered as ideal frictionless, then the pressure outside the cylinder at any angular position is given by

$$\frac{h_S - h_L}{(V^2/2g)} = 1 - 4\sin^2\theta \tag{2}$$

The fluids used in practical applications are not ideal; hence, the local pressure does not show the ideal behavior indicated by eq 2. Therefore, he measured reduction in local pressure by means of a manometer and correlated to the dimensionless parameter P' with the angular position of the orifice as a parameter, where

$$P' = \frac{h_S - h_L}{(V^2/2g)} \tag{3}$$

This was the first attempt at understanding the gas-induction process, in a fundamental manner, by looking at the local pressure. However, the relation between the impeller design, the impeller speed, and the local pressure was not established. The above equation was also not extended to the estimation of N_{CG}.

Evans et al. (1990, 1991) extended this earlier model of Martin (1972). The local liquid velocity was related

to the impeller speed as

$$U = (1 - K)2\pi NR \tag{4}$$

where K is a factor that accounts for the slip between the impeller and the fluid. The pressure coefficient C_P relating the local pressure $P(\theta)$ to the headspace pressure P_O was defined as

$$C_P(\theta) = \frac{(P_O + \rho_L gS) - P(\theta)}{\frac{1}{2}\rho_L U^2} \tag{5}$$

The pressure coefficient is a function of the blade shape and the orifice location. For inviscid flow, the value of $C_P(\theta)$ can be calculated from potential flow theory. For flow around a cylinder in an infinite medium its value, according to the above definition, is

$$C_P(\theta) = 4 \sin^2(\theta) \tag{6}$$

Since the actual geometry (rotating hollow pipe in a finite viscosity fluid) is far from this ideality, it becomes necessary to experimentally measure the values $C_P(\theta)$. The absolute pressure $P(\theta)$ on the blade surface can then be calculated by substituting eq 4 in eq 5. Further rearrangement gives

$$P(\theta) = (P_O - \rho_L gS) - \frac{1}{2}\rho_L C_P(\theta)[2\pi NR(1 - K)]^2 \tag{7}$$

At critical speed, the gas-induction process just begins and the local pressure equals the headspace pressure; that is, $P(\theta) = P_O$ and $N = N_{CG}$ and the above equation then gives

$$N_{CG} = \sqrt{\frac{gS}{2C_P(\theta)[(1 - K)\pi R]^2}} \tag{8}$$

The above equation was very successful in predicting the N_{CG} values for their system.

3.1.2. Type 12 and 22 Systems. White and de Villiers (1977) also started with Bernoulli's equation for predicting the critical impeller speed. They calculated the velocity head on the basis of impeller tip velocity and the pressure head was taken as the hydrostatic head. The final form of their equation is

$$\frac{N_{CG}^2 D^2}{gS} = C \tag{9}$$

Here, C is an empirical constant which is characteristic of the system. The value of the constant was found to be 0.23. The term on the left-hand side in the above equation is the Froude number, and hence the above equation can also be written as

$$Fr_{CG} = C \tag{10}$$

Sawant and Joshi (1979) have studied a wide variety of impellers and physical properties of the system. They have modified the above equation to take into account the effect of the liquid-phase viscosity. Their equation is given below:

$$\frac{N_{CG}^2 D^2}{gS}(\mu/\mu_w)^{-0.11} = \text{constant} = C \tag{11}$$

The value of the constant was found to vary between 0.21 ± 0.04, for a variety of different designs like pipe impellers (two pipes and four pipes), flattened cylindrical impellers, covered turbine impellers, Wemco flotation cells, Denver flotation cells, and shrouded turbine with a stator. The above equation was able to predict the critical speed for gas induction within 10% of the experimentally observed values. In this case, the constant C accounts for the nonidealities of the fluid, impeller slip, and frictional losses. The value of the constant is in agreement with that of White and de Villiers (1977).

Heim et al. (1995) have also used eq 10 for correlating their data on N_{CG}. Aldrich and van Deventer (1994) have investigated the effect of solid particles on N_{CG}. They have reported that N_{CG} is unaffected by the presence of solids up to a loading of 15%; beyond this value, the critical speed increases. This increase in N_{CG} was attributed to the increase in the viscosity of the solution because of the presence of solid particles.

Saravanan and Joshi (1995) have proposed a model based on the phenomena of forced vortex formation in the standpipe. As the impeller speed increases, the liquid level in the standpipe falls and takes the shape of a vortex. This is because the liquid present in the standpipe essentially behaves like a liquid in an unbaffled tank. They have proposed a mechanism of the gas-induction process as follows:

At speeds less than the critical speed, the vortex is formed. The vortex shape is paraboloid in nature (Figure 13A). As the speed increases, the vortex penetrates deeper and deeper, and at a critical impeller speed the vortex reaches the impeller tip (Figure 13B). The greater the impeller submergence, the greater the speed required for the vortex to reach the impeller tip. The critical speed for gas induction therefore is strongly dependent on the impeller submergence. Once the vortex reaches the impeller tip, bubble entrapment occurs, because of the small vortices generated at the interface. The mechanism is similar to that of surface aeration. The entrapped bubbles get conveyed away form the interface by the liquid flow generated by the impeller (Figure 13C). The gas-dispersion characteristics depend on the liquid flow pattern generated by the impeller which in turn depends on the geometrical features of the impeller and stator. A mathematical model was proposed by Saravanan and Joshi (1995), for the estimation of N_{CG} based on the following assumptions: (i) The gas-induction process occurs at the center plane of the impeller. The submergence of the impeller (S) and the impeller clearance from the bottom (C_1) are measured from the impeller center plane. (ii) Negligible resistance exists in the gas line connected to the standpipe.

The differential equation representing the tangential motion of the liquid is

$$dP = \rho_L f_m^2 \omega^2 r \, dr + \rho_L g \, dz \tag{12}$$

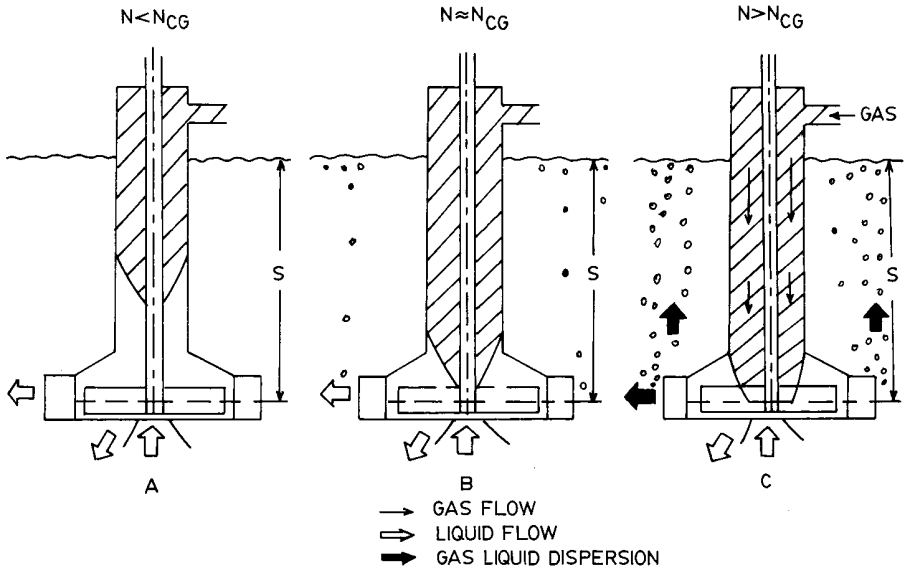

Figure 13. Vortex shapes formed in a stator−rotor system (courtesy, Saravanan and Joshi, 1995): (A) before the onset of gas induction, $N < N_{CG}$; (B) at the critical speed for gas induction, $N = N_{CG}$; (C) at a speed higher than N_{CG}.

with the boundary condition at $r = R$, $P = P_O$, and

$$z = \frac{k(Rf_m\omega)^2}{2g}$$

The z-direction increases in the vertically downward direction and the origin is at the intersection of the axis of the vessel and the static liquid level. Here, f_m is called the conformity factor, and it represents the slip between the impeller and the fluid surrounding it and is analogous to the "K" defined by Evans et al. (1990). Integrating eq 12 to any r and the corresponding P and z, and using this boundary condition, gives a relationship between the local pressure as a function of the radial position, and the vertical position z:

$$P - P_O = \frac{\rho_L f_m{}^2\omega^2}{2}(r^2 - R^2) + \rho_L g\left(z - \frac{k(Rf_m\omega)^2}{2g}\right) \quad (13)$$

The shape of the free surface of the vortex corresponds to a locus of all points with $P = P_O$; thus, the equation of the vortex surface is

$$z = \frac{(Vf_m)^2}{2g}\left((1 + k) - \frac{r^2}{R^2}\right) \quad (14)$$

Here $V = \omega R$ is the impeller tip velocity. The maximum depression occurs at the axis of the vessel corresponding to $r = 0$. At a critical speed this maximum depression equals the submergence of the impeller (i.e., the vortex reaches the impeller center plane). Setting $V = V_{CG}$ at this stage

$$S = \frac{(V_{CG}f_m)^2}{2g}(1 + k) \quad (15)$$

Let $(1 + k)f_m{}^2 = \phi$, where ϕ is the vortexing constant, and using $V_{CG} = 2\pi RN_{CG}$, we get

$$N_{CG} = \frac{1}{2\pi R}\sqrt{\frac{2gS}{\phi}} \quad (16)$$

This equation is very similar to that developed by White and de Villiers (1977). The above equation can also be written in terms of the Froude number, in a manner similar to that of eq 10; then the value of the constant turns out to be equal to 0.24, which is in excellent agreement with that of Sawant and Joshi (1979) and White and deVilliers (1977). The basic difference is that the constant ϕ is characteristic of the system, and it represents the ability of the impeller to form a vortex for a given impeller−standpipe−stator geometry. Using this equation Saravanan and Joshi (1995) were able to predict the values of N_{CG} for their single- as well as multiple-impeller systems within ±10%. Considering the complex nature of the two-phase flow and the fundamental nature of the model, the predicted values agree very well with the experimental data.

Patwardhan and Joshi (997) have investigated the effect of sparging on the critical impeller speed for gas induction. They have concluded that the change in the critical impeller speed ΔN_{CG} (N in the presence of sparging − N in the absence of sparging) depends only on the superficial gas velocity, the type of sparger, the lower impeller design, and so forth. That is,

$$\frac{(\Delta N_{CG})^2\pi^2D^2\phi}{2gS} = \alpha_1(C_3/D)^{\alpha_2}V_G{}^{\alpha_3}(S/T)^{\alpha_4} \quad (17)$$

They have reported the values α_1, α_2, α_3, and α_4 as a function of the sparger size and the lower impeller design. This equation is nothing more than a fit of the experimental data and should be used with extreme caution when applying to other systems and scales. However, if the critical parameters such as submergence and superficial gas velocity are similar to what has been used in their work, then the above equation may be used. The various models correlating the critical speed for gas induction are given in Table 3.

3.1.3. Recommendations. All the models for N_{CG} start with Bernoulli's equation, that is, eq 1. Equation 1 itself neglects the pressure loss occurring within the system. This also introduces a small amount of uncertainty in the analysis. Martin (1972) has really set the

Table 3. Critical Impeller Speed for Gas Induction

system investigated	basis for calculating N_{CG}, model	refs
pipe impellers (type 11)	Bernoulli's equation, measured pressure profiles	Martin (1972)
shrouded turbine (type 22)	$\frac{N_C^2 D^2}{gS} = K$	White and deVilliers (1977)
Denver and Wemco Flotation cells	$\frac{N_C^2 D^2}{gS}(\mu_w/\mu)^{0.11} = K$	Sawant and Joshi (1979)
hollow-bladed impeller (type 11)	Bernoulli's equation, pressure coefficient, blade slip factor	Evans et al. (1990)
hollow pipe	$Fr^* = \frac{N^2 d^2}{gS}$	Heim et al. (1995)
PBTD with stator and standpipe (type 22)	$N_{CG} = \frac{1}{2\pi R}\sqrt{\frac{2gS}{\phi}}$	Saravanan and Joshi (1995)
PBTD−stator, multiple impellers with sparging	$\frac{\Delta N_{CG}^2 \pi^2 D^2 \phi}{2gS} = \alpha_1 (C_3/D)^{\alpha_2} V_G^{\alpha_3} (S/T)^{\alpha_4}$	Patwardhan and Joshi (1997)

stage for understanding the gas-induction process by measuring the local pressure field. Evans et al. (1990, 1991) have made a valuable contribution by extending the measured pressure field to the estimation of N_{CG}. Although the type 11 impellers have been analyzed from a fundamental point of view, one important aspect has not really been dealt with. The measured local pressure field has not been related to the impeller geometry such as blade shape, blade width, impeller diameter, clearance, and so forth. When it comes to type 12 and type 22 impellers, the investigators have been more empirical than desired. At impeller speeds $N < N_{CG}$, the impeller rotates in the liquid-phase alone; thus, it should be possible to use an approach similar to the type 11 system, at least for the estimation of N_{CG}. Their equations for N_{CG} do include a balance between the pressure head and the velocity head, but no attempt has been made to experimentally measure or predict the pressure field. The approach of Saravanan and Joshi (1995) does start from the fundamental equations of motion. Inside the standpipe, their geometry behaves essentially like an unbaffled system; therefore, the vortex shape can be predicted fairly accurately. However, the assumption that the gas-induction process begins from the impeller centerline is not completely valid. The gas-induction process begins when the vortex is fairly close to the impeller but does not have to reach the impeller centerline. This has been pointed out by the authors and is reflected by a value of the constant $\phi < 1$. In summary, it can be said that the physics of the process of gas induction is fairly well-understood. One area that needs to be worked on is relating the impeller geometry (e.g., shape, width, diameter, clearance, etc.) to the local pressure field generated.

Figure 14 shows a comparison of the various correlations proposed for N_{CG}. The values of N_{CG} have been estimated on a scale of 0.5 m and an impeller diameter equal to one-third the vessel diameter. From the graph, it can be seen that the different impellers such as cylindrical, paddle, aerofoil, and disk show different values of N_{CG} under otherwise identical conditions. This is due to a difference in the local pressure field generated. A hollow paddle impeller shows the lowest value of N_{CG}. As expected, the correlations of White and deVilliers (1977), Sawant and Joshi (1979), and Saravanan and Joshi (1995) show similar values of N_{CG}. Keeping in mind the present status of knowledge, it is desirable to use the approach of Evans et al. (1990, 1991). However, if the impeller shape under investigation is drastically different from what they have used, then a good first approximation of the N_{CG} value can

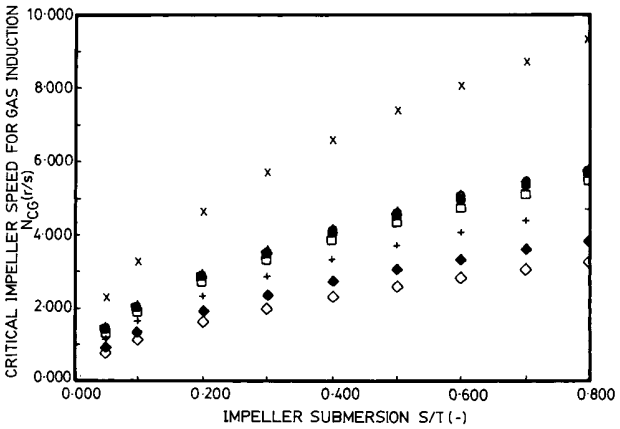

Figure 14. Comparison of different impeller designs for N_{CG}. All these have been evaluated at a tank diameter of 0.50 m and an impeller diameter $D = T/3$: ■, white and deVilliers (1977); ♦, Evans et al. (1990), cylinder; ◇, Evans et al. (1990), paddle; ×, Evans et al. (1990), aerofoil; △, Saravanan and Joshi (1995); □, Sawant and Joshi (1979); +, Heim et al. (1995), four-pipe impeller; ○, Heim et al. (1995), disk impeller.

be obtained by using the correlation of White and de Villiers (1977) and the value of the constant between 0.21 and 0.25, or the correlation of Saravanan and Joshi (1995). The latter correlation is useful for scale-up because it has been tested over a wide range of equipment sizes (0.57−1.5 m).

3.2. Gas-Induction Rate. 3.2.1. Type 11 Systems. A type 11 system involves the flow of gas alone through the impeller. The driving force for the gas induction is the pressure differential between the headspace and the local pressure at the orifice on the impeller. The flow of gas causes frictional and resistive pressure drop in the hollow pipe, blades, and the orifice. If the pressure differential generated by the impeller for the gas flow is equated to the total resistive pressure drop, then the rate of gas induction can be calculated.

Martin (1972) has measured the local pressure around the hollow pipe impeller and has correlated it empirically to the gas-induction rate, using the orifice discharge coefficient. The basis for using such an equation is the analogy with the flow in a pipe containing an orifice. The use of this equation implies fully developed turbulent flow conditions in a pipe with a uniform cross section. These conditions can hardly be expected to be fulfilled in a hollow pipe impeller assembly. The equation also neglects the change in the gravity head. The orifice discharge coefficient characterizes the frictional pressure drop occurring in the hollow pipe. The second

term is used mainly as a fitting parameter. Since the values of C_O, A_O, K_1, and so forth vary with the design of the hollow shaft, orifice, and the blade design, caution has to be exercised while using this equation.

$$Q_G = C_O A_O K_1 [2g(-h_S)(\rho_L/\rho_G)]^{1/2} - 0.00085K_1 \qquad (18)$$

where h_S is given as

$$\frac{h_S - h_L}{(V^2/2g)} = P' \qquad (19)$$

and V is the impeller tip velocity ($V = 2\pi NR$). K_1 can be considered as a flow correction factor which depends on the angular position of the orifice.

Raidoo et al. (1987) have observed that the pressure driving force in the presence of gas induction was lower than the pressure driving force in the absence of gas induction by a factor as much as 10−20. The velocity head generated by the impeller depends on the density in the impeller region. When the gas is induced, the average density in the impeller region decreases substantially ($\bar{\rho} = \rho_L\epsilon_L + \rho_G\epsilon_G \approx \rho_L\epsilon_L$). Therefore, the velocity head generated by the impeller is substantially lower in the presence of the induced gas. Therefore, the pressure driving force (headspace pressure − pressure near the orifice) decreases substantially due to the presence of gas. The average density in the impeller region is very important. The average density in the impeller region depends on the local fractional gas holdup. This in turn depends on the rate at which gas is induced and the rate of gas dispersion. If the latter is high, then the local density will practically be the same as the liquid density, and therefore the gas induction may not decrease the pressure driving force substantially. Whereas, if the former is higher, then the gas holdup in the impeller region and the reduction in the pressure driving force due to the induced gas will be substantial.

Baczkiewicz and Michalski (1988) have given an empirical correlation for the maximum value of the ratio Q_G/V_L. This correlation arises from a data fitting exercise; it does not consider the physics of the process occurring.

$$(Q_G/V_L)_{max} = (2.36 \times 10^{-4})N^{1.53}(D/T)^{1.83}n_P{}^{0.26} \qquad (20)$$

Evans et al.(1990) equated the pressure driving force generated by the impeller rotation to the pressure drops for the flow of gas in the hollow-bladed impellers (orifice equation) and the hollow shaft and proposed the following equation for the gas-induction rate. Since the starting point is the orifice equation, it has the same limitations that were given earlier.

$$Q_G = C_O A_O \sqrt{\frac{2[P_O - P(\theta)]}{\rho_G}} \qquad (21)$$

Substituting for $[P_O - P(\theta)]$ from eq 7, we get

$$Q_G = C_O A_O \sqrt{\frac{\rho_L}{\rho_G}[C_P(\theta)(2\pi RN(1-K))^2 - 2gS]} \qquad (22)$$

The above equation grossly overpredicts the gas-induction rate. At speeds of $N > N_{CG}$, gas induction occurs and the average density in the impeller region decreases substantially. After the gas induction begins, the local pressure was related to the impeller speed using the average density. Equation 7 was thus modified to give the following equation:

$$P(\theta) = (P_O + \rho_L gS) - \frac{1}{2}\overline{\rho_L} C_P(\theta)[2\pi NR(1-K)]^2 \qquad (23)$$

The average density is defined as $\bar{\rho} = \rho_L(1 - \epsilon_G)$; substituting eq 23 in eq 21, the following equation is obtained:

$$Q_G = C_O A_O \sqrt{\left(\frac{\rho_L(1-\epsilon)}{\rho_G} + \epsilon\right) C_P(\theta)[2\pi RN(1-K)]^2 - \frac{2\rho_L gS}{\rho_G}} \qquad (24)$$

The above equation was fairly successful in predicting the gas-induction rate for a variety of different operating conditions, like the gas feed to the central shaft or the riser tube, effect of submersion depth, and so forth. Their prediction for Q_G versus N was good at high speeds but relatively poor at low speeds. This basic model was progressively modified by the authors taking into account the various processes occurring, such as the frictional pressure drop in the hollow pipe, the pressure drop associated with the kinetic energy imparted to the liquid for the formation of the bubble, the pressure drop required to overcome the surface tension forces for the formation of bubbles, and so forth.

Evans et al. (1991) and Rielly et al. (1992) proposed that the net driving force for the gas induction is $\Delta P_T = [P_O - P(\theta)]$ which is generated by the impeller rotation and can be expressed by eq 7 above:

$$\Delta P_T = \frac{1}{2}\rho_L C_P(\theta)[2\pi RN(1-K)]^2 - \rho_L gS \qquad (25)$$

whereas the various resistances responsible for the pressure drop as the gas flows from the headspace into the liquid are (1) ΔP_P = frictional pressure drop along the gas pathway $\propto Q_G$; (2) ΔP_O = orifice pressure drop; (3) ΔP_{KE} = pressure drop associated with the kinetic energy imparted to the liquid, $= (3Q_G{}^2\rho_L)/(32\pi^2 r_b{}^4)$; (4) ΔP_σ = pressure drop required to overcome the surface tension forces at the orifice, $2\sigma/r_b$. The rate of gas induction at steady state can be obtained by equating the net driving force to the sum of all the resistances. The balance is given by the following equation:

$$\Delta P_T = \Delta P_P + \Delta P_O + \Delta P_{KE} + \Delta P_\sigma \qquad (26)$$

The expressions for ΔP_{KE} and ΔP_σ assume that a single spherical bubble is getting formed in a stagnant liquid. At high gas flow rates, the shape of gas bubbles may deviate from the spherical; likewise, a stream of gas bubbles may also be formed. In that case, the present expressions ΔP_{KE} and ΔP_σ may not hold. One of the basic limitations of this approach is that the pressure coefficient $C_P(\theta)$ must be known.

Rigby et al. (1994) have measured the pressure profiles in the liquid behind the impeller blades. They have found that the pressure driving force reached a maximum slightly off the blade surface in the wake region behind the blade. Locating the orifice at such a location increased the gas induction rates by 5−10% as compared to the orifice located on the blade surface. Forrester and Rielly (1994) also used the pressure

Table 4.

A. Models for the Rate of Gas Induction for the Type 11 System

impeller type	basis for the prediction of Q_G	accuracy	refs
hollow pipe and flattened pipe impeller	empirical, flow correction factor K_1		Martin (1972)
hollow pipe	$(Q/V_L)_{max} = 2.36 \times 10^{-4} n^{1.5}(d/D)^{1.8} i^{0.26}$		Baczkiewicz and Michalski (1988)
hollow-bladed impeller	blade slip factor K and pressure coefficient $C_P(\theta)$	10%	Evans et al. (1990)
hollow-bladed impeller	K, $C_P(\theta)$, and $\Delta P_T = \Delta P_P + \Delta P_O + \Delta P_{KE} + \Delta P_\sigma$	20%	Evans et al. (1991)
two-bladed disc turbine orifice behind and off the blades	K, $C_P(\theta)$ and $\Delta P_T = \Delta P_P + \Delta P_O + \Delta P_{KE} + \Delta P_\sigma$	20%	Evans et al. (1994)
hollow-bladed with multiple orifices	K, $C_P(\theta)$ and $\Delta P_T = \Delta P_P + \Delta P_O + \Delta P_{KE} + \Delta P_\sigma$	20%	Forrester et al. (1994)
hollow pipe	$\frac{K_G}{K_{G\infty}} = 1 - \exp(-CRe^{c_1} Fr^{*c_2})$		Heim et al. (1995)
hollow-bladed with multiple orifices	similar to Evans et al. (1991), Forrester et al. (1994)		Forrester et al. (1998)

B. Models for the Rate of Gas Induction for Type 12 and 22 Systems

impeller type	model for the rate of gas induction	refs
Wemco machine	$Q_g \propto D^{2.4} \ln(N)$	Degner and Treweek (1976)
slotted pipe stator, pump rotor	$NQ_g\sqrt{D/S'} = 0.0231(Fr' - Fr'_c)^{1.84}$	White and de Villiers (1977)
Wemco machine	$Q_g = 51.2(Fr - Fr_c)^{0.83}(D/S)^{0.5}$	Sawant et al. (1980)
Denver machine	$Q_g = 0.0021(N^2 - N_c^2)^{0.75} D^3$	Sawant et al. (1981)
multiple-impeller system	$V_i = 7.15 \times 10^{-6} N^{1.9} D^{3.95} T^{-0.25} \sigma^{-2.4} \mu^{-0.15}$	Matsumura et al. (1982a)
PTD rotor with stator	$Q_g^2 = 2.68 \times 10^{-4} (\Delta P D^2)^{1.184}$	Raidoo et al. (1987)
PBTD with stator	$Q_g = \lambda^* N R^2 \left[1 - \frac{2gS}{\phi V^2}\right] + \alpha^* N R^3 \left[1 - A\left(\frac{2gS}{\Phi V^2}\right)\right]^{3/2}$	Saravanan and Joshi (1995)
PBTD−stator, multiple impellers with sparging	$1 - \frac{Q_{GS}}{Q_G} = \beta_1 Fl^{\beta_2} (C_3/D)^{\beta_3}$	Patwardhan and Joshi (1997)

balance model developed by Evans et al. (1991) and modified it for the case of multiple orifices located on a single blade. By using four orifices, the rate of gas induction was found to increase by a factor of 3 at an impeller speed of 9 rps as compared to just a single orifice. They were able to predict the gas induction rates within 20% of the experimental values.

In a recent work Forrester et al. (1998) have proposed further improvements on this model. The first modification enables good predictions at speeds close to N_{CG}. This is done by allowing the bubble size to be equal to the orifice size at speeds close to N_{CG}. In the earlier model of Evans et al. (1991), the pressure loss due to kinetic energy imparted to the liquid was calculated on the basis of the bubble formation in an infinite stagnant liquid. In this work, this pressure loss term was modified by applying potential flow solution for an expanding sphere. These modifications enabled much better predictions of the gas-induction rate as compared to those of Forrester et al. (1994).

Heim et al. (1995) have investigated four and six hollow pipe impellers and a hollow disk impeller. They have correlated the gas-induction rate with Reynolds number and Froude number. Their correlation is as follows:

$$\frac{N_{QG}}{N_{QG\infty}} = 1 - \exp(-CRe^{c_1} Fr^{c_2}) \tag{27}$$

Since this is a fit of the experimental data, it is essential to consider the range of Re and Fr covered by the authors. Table 4A gives a summary of the various models proposed for type 11 systems.

3.2.2. Type 12 and 22 Systems. Type 12 and 22 systems involve the two phases gas and liquid. The hydrodynamics is complicated and is less amenable to theoretical analysis, mainly because the complex two-phase hydrodynamics is poorly understood. For a gas-inducing impeller, the gas induction rate is zero at the critical impeller speed. As the impeller speed increases above N_{CG}, the velocity head generated by the impeller increases as $(N - N_{CG})^2$ or $(N^2 - N_{CG}^2)$. The gas-induction rate should be proportional to the pressure difference created (i.e., velocity head generated), and hence several empirical correlations for Q_G include terms such as $(N - N_{CG})^a$ or $(N^2 - N_{CG}^2)^b$. White and de Villiers (1977), Sawant et al. (1980, 1981), and Aldrich and van Deventer (1994, 1996) have used such terms for correlating their data. Their correlations are listed in Table 4B.

Zundelevich (1979) attempted to model the gas-induction rate of a turboaerator by drawing an analogy to a liquid jet gas ejector with the following assumptions: (i) The gas induction was assumed to be occurring because of the action of the liquid flow coming out of the impeller periphery. (ii) The impeller liquid flow number (η) was assumed to be constant at all speeds. (iii) The proportion of the induced gas flow rate to the liquid flow rate was assumed to be the same as that for a geometrically similar water jet ejector. (iv) An empirical equation for the water jet ejector (correlating the ratio of the liquid and the gas flow rates to the pressure differential and the mixing chamber pressure differential) was assumed to be valid for the gas-inducing impeller.

With these assumptions, he showed a unique relationship to exist between the two dimensionless parameters, namely, the impeller head coefficient (C_H) and the gas Euler number (Eu_G):

$$1 + \eta\sqrt{Eu_G/C_H} = 3\sqrt{\eta^2 Eu_G/C_H - 3\eta^2\left(\frac{Eu_G}{C_H + \frac{k}{2}\pi^2}\right)} \tag{28}$$

where $Eu_G = gS/(Q_G/D^2)^2$ and $C_H = gS/(ND)^2$.

Zundelevich (1979) proposed that this relationship could be used in the scale-up of these impellers. However, Raidoo et al. (1987) tried to correlate their data for 0.15-, 0.20-, and 0.25-m diameter impellers using the above correlation. They have observed that such a unique correlation between C_H and Eu_G did not exist.

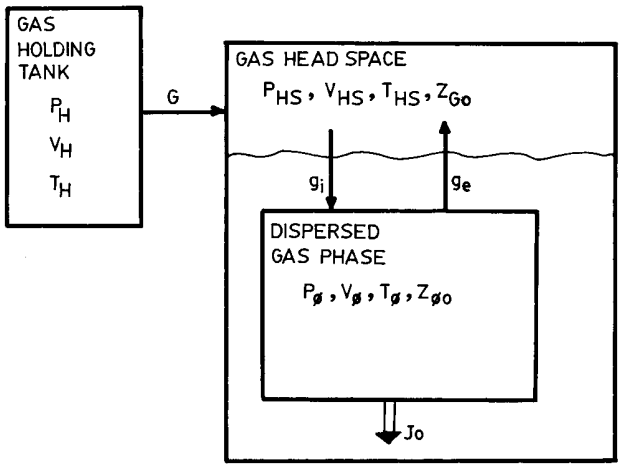

Figure 15. Schematic representation of the experimental setup of Matsumura et al. (1982a).

This could be because of the several overly restrictive assumptions used in the model like constancy of the impeller flow number, equivalency of the liquid jet ejector, and a gas-inducing impeller, and so forth. The induced gas would tend to form cavities behind the impeller blades, causing a reduction in the impeller pumping capacity. In summary, the assumptions made are not representative of the reality. The basic equation used in deriving eq 28 is an empirical equation for the liquid jet ejector which in itself does not represent the physical picture.

The pressure balance approach used for type 11 systems was extended by Raidoo et al.(1987) for type 22 systems (shrouded disk turbine; shrouded curved blade turbine; PBTD). Starting from Bernoulli's equation, they correlated the experimentally measured pressure drops to the impeller tip velocity, for different H/T ratios. This equation neglects the frictional pressure drop occurring:

$$\Delta P_T + \rho_L g S = \alpha[\rho_L(\pi D N)^2/2]^\beta \tag{29}$$

The constants α and β were experimentally evaluated for H/T ratios of 1.0, 0.75, and 0.6. The ΔP predicted from eq 29 was correlated to the gas-induction rate empirically by the following equation:

$$Q_G{}^2 = (2.68 \times 10^{-4})(\Delta P D^2)^{1.184} \tag{30}$$

Matsumura et al. (1982a,b) have investigated a multiple-impeller system. The upper impeller was designed for bubble entrapment and the lower impeller was designed for bubble dispersion. The lower impeller was always operated at the speed required for the dispersion of the bubbles entrapped by the upper impeller. They have determined the gas-induction rate by a chemical method. The liquid under investigation was a sodium sulfite solution containing a cobalt catalyst. The kinetics of the reaction were established. A mixture of oxygen and nitrogen was taken in the headspace. As the impeller rotates, gas is induced and the oxygen reacts with the sodium sulfite. A pressure-controlling device on the reactor supplies oxygen at the rate at which it is consumed. Their experimental setup is shown schematically in Figure 15. The rate of gas induction is found in the following manner. The gas and the liquid phases were assumed to be well-mixed and the material balance equations were written as follows:

material balance for the oxygen in the holding tank

$$V_H \frac{d}{dt}(P_H/R_G T_H) = -G \tag{31}$$

material balance for oxygen in the headspace

$$V_{HS} \frac{d}{dt}(P_{HS} z_{GO}/R_G T_{HS}) = G - (g_i z_{GO} - g_e z_{\phi O}) \tag{32}$$

material balance for oxygen in the dispersed gas phase

$$V_\phi \frac{d}{dt}(P_\phi z_{\phi O}/R_G T_\phi) = (g_i z_{GO} - g_e z_{\phi O}) - V_L J_O \tag{33}$$

Oxidation of sodium sulfite in the presence of a cobalt catalyst is zero-order with respect to sodium sulfite. Using the theory of mass transfer accompanied by chemical reaction (Doraiswamy and Sharma, 1984), the rate of oxygen uptake can be written as $R_A\underline{a} = \sqrt{M}k_L\underline{a}[A^*]$. The quantity $\sqrt{M}$ can be defined in the following manner:

$$\sqrt{M} = \frac{\sqrt{\frac{2}{m+1} D_O k_{mn} [A^*]^{m-1} [B_O]^n}}{k_L}$$

Substituting for the orders of the reaction, that is, $m = 2$ and $n = 1$, gives

$$\begin{aligned} J_O &= -V_H \frac{d}{dt}(P_H/RT_H) = (g_i z_{gO} - g_e z_{\phi O}) \\ &= V_L \underline{a} \sqrt{2/3 k_{2,0} D_O} (P_{\phi z \phi O} H_O)^{3/2} \end{aligned} \tag{34}$$

Further, assuming that the nitrogen gas is in equilibrium with the gas and the liquid phases and that $g_i(1 - z_{GO}) = g_e(1 - z_{\phi o})$, the following relations were obtained by them:

$$\frac{z_{\phi O}}{z_{GO}} = (1 - \xi_O)/(1 - \xi_O z_{GO}) \quad \text{and} \quad g_e/g_i = 1 - \xi_O z_{GO} \tag{35}$$

where the fraction of the absorbed oxygen is denoted by ξ_O.

$$\xi_O = (1 - g_e z_{\phi O}/g_i z_{GO}) \tag{36}$$

Assuming $P_{HS} = P_\phi$,the following relation was derived:

$$\begin{aligned} J_O &= -\frac{V_H}{V_L} \frac{d}{dt}\left(\frac{P_H}{RT_H}\right) \\ &= \frac{1}{V_L} \xi_O g_i z_{GO} \end{aligned} \tag{37}$$

The molar volumetric absorption rate J_O can be obtained from the pressure changes in the gas holder. If the interfacial area per unit volume is measured, then the value of ξ_O can be calculated. Knowing J_O and ξ_O, and z_{GO} (which was also measured), the molar flow rate of the induced gas (g_i) can be calculated. This can then be converted to the volumetric flow rate. The gas-induction rate was correlated to the upper impeller speed, upper impeller diameter, tank diameter, and the

physical properties of the system with an empirical equation. Since the lower impeller speed was not varied, the variation of the gas-induction rate with it cannot be determined.

Mundale and Joshi (1995) have investigated a large number of designs of rotors for their stator−rotor system. These designs were basically of the pitched blade downflow turbine (PBTD) type. A number of variations were investigated (viz. blade angle from 30 to 90°, blade angle varying from hub to tip, number of blades, blade thickness, curvature along the blade width, curvature along the blade length, blade width, perforated blades, and so forth). They have recommended the use of a 45°, six-bladed PBTD impeller with a blade width of one-third of the impeller diameter. They further recommend that a close match between the stator and the rotor is essential for good performance. They have observed that the performance of the impeller is drastically affected by any axial or radial obstructions to the flow coming into the impeller.

Saravanan and Joshi (1995) have extended their forced vortex formation model to predict the gas-induction rate. They have proposed that the overall gas-induction process occurs in two steps, namely, bubble entrapment and bubble carriage. They have assumed that the rate of gas-bubble entrapment is proportional to the product of the area of intersection of the vortex with the impeller center plane and the impeller speed. The proportionality constant was denoted as the gas-induction modulus (λ) and it denotes the ability of the impeller to generate and entrap gas bubbles from the vortex. Physically, it represents the thickness of the gas film imbibed into the liquid for every revolution of the impeller. The gas−liquid interfacial area was assumed to be proportional to the area of intersection of the vortex with the impeller center plane that is πX^2. The radius of intersection X is depicted in Figure 13C.

$$Q_G = \lambda N \pi X^2 \tag{38}$$

Rearranging eq 14 in terms of r^2/R^2 and denoting $r = X$ at the impeller center plane,

$$\frac{X^2}{R^2} = (1 + k_g)\left(1 - \frac{2gS}{\phi V^2}\right) \tag{39}$$

Substituting for X^2 in eq 38 using eq 39 and denoting $\lambda^* = \pi\lambda(1 + k_g)$,

$$Q_E = \lambda^* N R^2 \left(1 - \frac{2gS}{\phi V^2}\right) \tag{40}$$

The rate of the bubble carriage was considered to be proportional to the liquid pumping rate, given as

$$Q_C = \alpha^* N R^3 \left(1 - A\left(\frac{2gS}{\phi V^2}\right)^{3/2}\right) \tag{41}$$

In reality, the steps of bubble entrapment and bubble carriage occur in series. However, when the series mechanism was fitted to the experimental data, poor fit was observed. Hence, they have attempted to fit the data assuming that these steps occur in parallel. This gave a better fit to the experimental data. In reality, these two steps do occur in series. This is one of the obvious limitations of this early work. It is also likely that the rate-controlling step changes from the center to the tip of the impeller: entrapment-controlled in the central region and carriage-controlled in the tip region. Therefore, the essentially series mechanism may look parallel. In our laboratory, further work is being done to throw more light on the rates of these two processes, which may ultimately result in a better model that is consistent with the reality as well as with the experimental data. The final expression of the model is given below:

$$Q_G = \lambda^* N R^2 \left(1 - \frac{2gS}{\phi V^2}\right) + \alpha^* N R^3 \left(1 - A\left(\frac{2gS}{\phi V^2}\right)^{3/2}\right) \tag{42}$$

The values of the constants λ^*, α^*, and ϕ were obtained by regression analysis of a large amount of experimental data in 0.57-, 1.0-, and 1.5-m diameter vessels. The constants in the above equation characterize the system in terms of the ability of the impeller to generate the vortex (ϕ), the ability of the impeller to convert the unstable vortex shape into a gas−liquid dispersion (λ^*), and the impeller pumping constant (α^*). They were able to predict the values of gas-induction rates to within 15% of the experimentally measured values. In this model, the empiricism is introduced through the values of λ^* and α^*. The key assumption of Q_E being proportional to the product of the area of intersection of the vortex and the impeller speed needs to be investigated further. Similarly, the bubble carriage rate is taken as a function of the liquid flow alone.

Table 4B gives an overview of the various models used to predict the gas-induction rate.

3.2.3. Multiple-Impeller Systems. Saravanan and Joshi (1995) have extensively investigated multiple-impeller systems. They have reported that the PBTD−PU and PBTD−PBTU combinations give the highest gas-induction rate for a given power consumption. This was attributed to the flow characteristics of the bottom impeller. The PU or PBTU impeller at the bottom generates an axially upward flow and this causes an increase in the amount of liquid reaching the gas-inducing impeller. Thus, the capacity of the liquid to carry away the gas bubbles increases. The rate of gas induction therefore increases. Whereas a PBTD impeller at the bottom withdraws liquid from the upper gas-inducing impeller. The bubble carriage capacity decreases, and the gas-induction rate also decreases. The liquid-phase flow pattern and gas-dispersion characteristics with different designs of the lower impeller are shown in Figures 16, parts A−C. It can also be seen that a lower PBTU impeller also improves the dispersion of the induced gas (Figure 16B). The values of λ^* and α^* were reported for single- and multiple-impeller systems with different designs of the lower impeller. They have reported that the λ^* values are essentially unaffected by the lower impeller design. Its value is around 130 for the various systems investigated by them. The value of α^* depends strongly on the lower impeller design. The value of α^* for a single-impeller system is 92.42. When a PBTU impeller is used at the bottom, this value increases to 212, indicating that the bubble carriage capacity is increased considerably. When the PBTD impeller is used at the bottom, the value of α^* decreases marginally to 86, indicating a decrease in the bubble carriage capacity and hence a reduction in the gas-induction rate. The design of the lower PBTU was optimized by varying the blade angle, blade width, number of blades, diameter, clearance, and so forth.

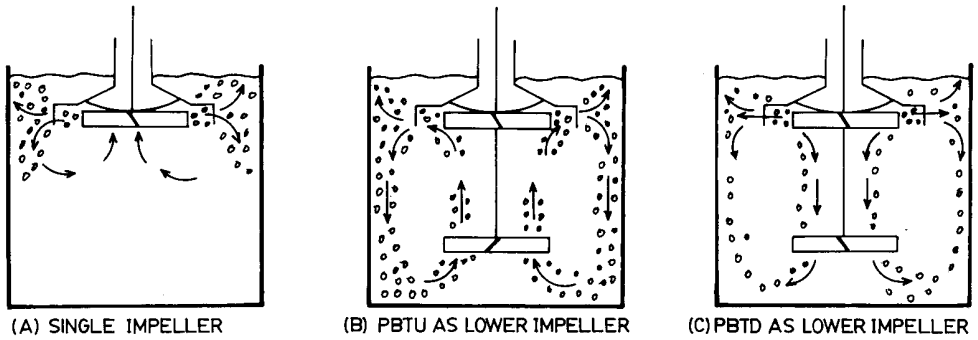

Figure 16. Liquid-phase flow pattern and gas-dispersion characteristics for different designs of the lower impeller: (A) single gas-inducing impeller; (B) PBTU as the lower impeller; (C) PBTD as the lower impeller.

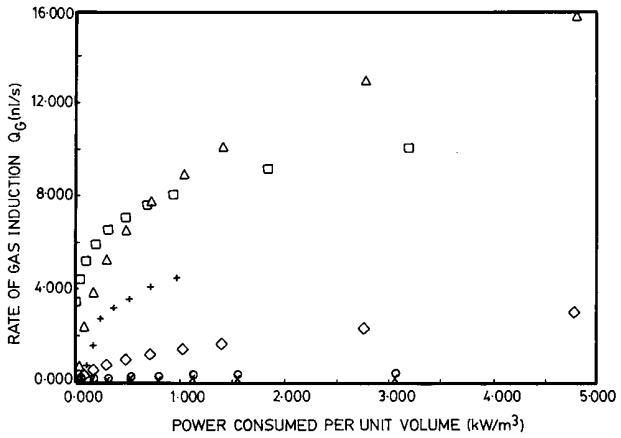

Figure 17. Comparison of gas-induction characteristics of different designs of gas-inducing impellers: △, Saravanan and Joshi (1995); □, Raidoo et al. (1987); +, Joshi and Sharma (1977); ◇, Aldrich and van Deventer (1994); ○, Sawant et al. (1981); ×, Sawant et al. (1980); ●, Heim et al. (1995).

Patwardhan and Joshi (1997) have investigated the multiple-impeller system of Saravanan and Joshi (1995) in conventional stirred vessels. The effects of sparger design, superficial velocity of the sparged gas, the lower impeller design, and so forth were investigated and the rate of gas induction in the presence of sparging was correlated empirically with the following equation:

$$1 - \frac{Q_{GS}}{Q_G} = \beta_1 Fl^{\beta_2}(C_3/D)^{\beta_3} \qquad (43)$$

Since this is a completely empirical equation, care has to be taken while using this equation for other systems and scales.

3.2.4. Recommendations. Figure 17 compares the rate of the gas induction of various types of impellers reported in the literature. In this figure, the different types of gas-inducing impellers have been evaluated on a common basis, namely a tank size of 0.5 m, D/T ratio equal to 0.33, and impeller submergence equal to 0.1 m. From the figure, it can be seen that the gas-induction characteristics of the multiple-impeller system PBTD−PU are far superior as compared to any other design previously reported. Thus, for gas-induction purposes, such multiple-impeller systems are highly recommended. In such systems the upper impeller can be located very close to the free liquid surface ($S = 100-200$ mm), to maintain a high rate of gas induction. The second impeller situated well-below the gas-inducing impeller is responsible for the generation of a favorable flow field in the liquid phase for efficient gas dispersion. Such a multiple-impeller system therefore ensures both a high gas-induction rate as well as good gas-dispersion characteristics. The design of the second impeller can be optimized to suit any desired design objective like heat transfer, solid suspension, mixing, gas dispersion, and so forth.

The prediction of the gas-induction rate (Q_G) is more difficult than that of the critical impeller speed. In type 11 systems the flow through the impeller zone consists of single gas phase. This can be considered analogous to the flow of gas through a pipe with various resistances. The models developed by Evans et al. (1991) and Rielly et al. (1992) take into account the various resistances for the flow of the gas phase and the driving force (pressure drop) generated by the impeller. Their model is thus based on fundamental principles and can be used for a priori estimation of the gas-induction rate. What remains to be tackled in such an approach is relating the local pressure coefficient to the impeller geometry and the speed in a fundamental manner. If this is achieved, then the gas-induction rate for a type 11 system can be predicted completely from fundamental principles. Such an exercise would also be suitable for the optimization of the impeller design. When type 11 systems are being considered, their approach is highly recommended for rational design. It would be interesting to compare the effects of blade shape, number of blades, orifice location on the gas holdup, or the rate of gas induction on the basis of equal power consumption. But such a comparison is not possible because the data on power consumption (power number and its variation with gas flow rate) are not available for type 11 systems. It is desirable to carry out systematic experimental investigations on the effect of orifice location, size and shape of the pipes, number of pipes, and so forth on the power consumption in both gassed and ungassed states, and simultaneously measure the rate of gas induction, fractional gas holdup, and so forth. Such an exercise will serve as a basis for the selection of optimum geometry of type 11 systems.

Type 12 and 22 systems pose more difficulties as they involve the flow of a gas and liquid through the gas-inducing impeller. The flow pattern in the liquid phase itself can influence the gas-induction rate. Saravanan and Joshi (1995) have proposed that the process of gas induction depends on the bubble entrapment and bubble carriage rate. However, further work is still needed in elucidating the effect of impeller design and operating conditions on the flow field generated and in turn the rates of bubble entrapment and bubble carriage and their interrelation. Until such an understanding can be developed, their correlation is recommended for scale-

up, mainly because the experiments have been carried out on fairly large vessels of different sizes (i.e., 0.57, 1.0, and 1.5 m) and over a wide range of impeller geometries and operating conditions.

3.3. Power Consumption. 3.3.1. Type 11, 12, and 22 Systems. Power consumption in stirred vessels and equipment of this kind contributes significantly to the utility cost. The power drawn by the impeller is consumed for various purposes, namely the generation of bulk liquid flow, generation of turbulence, dispersion of induced gas, solid suspension, heat transfer, mixing, and so forth. Thus, power consumption has a direct influence on the performance of the reactor.

Flotation machines were investigated primarily to generate the data for scale-up. Several workers have tried to correlate the power consumption (in terms of the power number, N_P)with the dimensionless quantities such as *Re*, *Fr*, N_Q, and so forth. [Arbiter et al. (1969), Fallenius (1981), and Schubert and Bischofberger (1978)]. Researchers who were interested in comparing the gas-inducing impellers with conventional mechanically agitated contactors have empirically correlated the ratio of power in the gassed state as compared to the ungassed state, with the gas flow rate, the design details of the impeller, and the operating variables [Topiwala and Hamer (1974) and Joshi and Sharma (1977)]. In any case much of the literature on the power consumption of gas-inducing impellers is empirical.

There is an agreement in the literature among various workers that the power consumption in the gassed state is lower than that in the ungassed state. This reduction in power consumption can be explained by the following two reasons. (i) Cavity formation: The induced gas forms cavities behind the impeller blade; this makes the liquid flow around the impeller blades more stream lined, thereby reducing the drag and causing a reduction in the power consumption. Grainger-Allen (1970) gives excellent photographic evidence of cavity formation behind the impeller blades. (ii) Gas recirculation: Because of the flow pattern generated by the impeller, a certain amount of gas gets recycled in the vessel. The average density in the impeller vicinity decreases, causing a decrease in the power consumption.

One of the earliest models for the power consumption was developed by Arbiter et al. (1969). The following assumptions were made in their model. (i) The density of the gas−liquid dispersion was assumed to be a weighted mean of the gas and liquid densities. (ii) The ratio of the liquid flow generated by the impeller to the rate of gas induction was related to the gas flow number, through an empirical relationship obtained by experiments on a centrifugal pump. This relationship was assumed to be valid for gas-inducing impellers. On the basis of these assumptions they derived the following equation:

$$\frac{P_G/P_L}{1 - P_G/P_L} = \frac{\rho_a}{\rho_L}(\alpha(1/N_{QG})^n + \beta) \qquad (44)$$

The second assumption of the application of the centrifugal pump equation to the gas-inducing impeller is not completely justified. The gas-inducing impeller generates both gas flow (induction) and a liquid flow. In this sense it is different from a centrifugal pump. The empirical nature of the correlation is evident from eq 44.

Topiwala and Hamer (1974) and Joshi and Sharma (1977) have investigated hollow pipe impellers and have correlated the power consumption with the help of an empirical relationship developed by Michel and Miller (1962) and it is given by the following equation:

$$P_G = C(P_L{}^2 N D^3/Q_G{}^{0.56})^{0.45} \qquad (45)$$

Joshi and Sharma (1977) have reported the value of the constant C as 0.364 for the pipe impellers with two pipes. They further report that, at low gas flow rates the value of the constant C becomes sensitive to Q and is lower than 0.364. The correlation of Michel and Miller (1962) is fairly popular in the field of stirred vessels. One of the basic differences between a stirred vessel and a gas-inducing impeller is that, in the latter the induced gas flow rate cannot be varied independently. The gas-induction rate is intimately lined to the impeller speed (power consumption), the impeller design, and geometry. The equation is empirical and caution has to be exercised while using it.

Zundelevich (1979), drawing an analogy between the gas-inducing impeller and a jet loop reactor, derived an expression for the rate of gas induction in terms of the impeller head coefficient and the gas Euler number. He derived a relationship in terms of the gas-induction rate per unit power consumption (Q_G/P_G). Assuming that the impeller power number is constant and using an average density of the dispersion, the parameter Q_G/P_G was related by

$$\frac{Q_G S}{P_G} = \frac{C_H}{N_P \rho g}\left(\frac{N_{QG}{}^2}{\eta} + N_{QG}\right) \qquad (46)$$

The optimum value of the ($Q_G S/P_G$) was 1.08×10^{-5} $m^4/W{\cdot}s$ for the air−water system, and the values of the constants were $N_P = 3.1$ and $\eta = 0.071$. The above correlation also suffers from the limitations mentioned in the earlier section.

Matsumura et al. (1982a) have correlated the power consumption in their multiple-impeller system with the Reynolds number and the Froude number of the upper impeller. The power consumption was also correlated in an alternate form using the gas-induction rate. Since the correlation is empirical, care has to be taken while applying the correlation beyond the ranges investigated by the authors.

Baczkiewicz and Michalski (1988) have investigated hollow pipe impellers and have correlated the gassed power consumption with the following equation:

$$P_G/V_L = 0.62 N^{3.44}(Q/V_L)^{-0.31}(d/D)^{4.48} n_P{}^{1.07} \qquad (47)$$

Saravanan et al. (1996) have made a first attempt at modeling the power consumption in terms of the drag force acting on the blade. In the absence of induced gas ($N < N_{CG}$), they have modeled the power consumption in the absence of gas induction in the following manner. The flow pattern generated by the single gas-inducing impeller is seen in Figure 16A. It can be seen that, below the impeller, there is an inflow. This inflow of liquid could exert a drag force on the gas-inducing impeller. This drag force was assumed to result in a constant torque τ_r. The slip factor which accounts for the slip of the impeller blade and the liquid was assumed to be constant over the entire blade length.

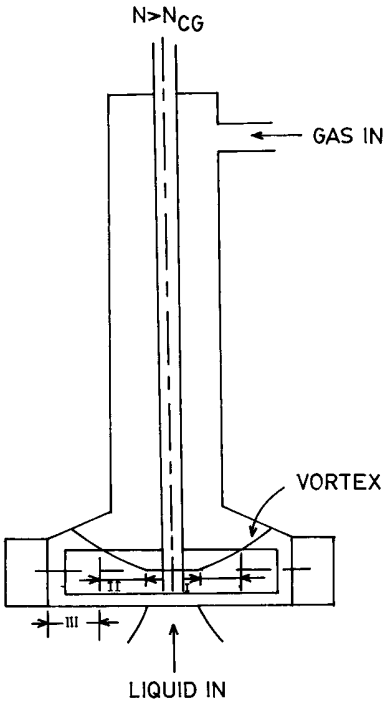

Figure 18. Vortex model for the prediction of power consumption (courtsey, Saravanan et al., 1996). (I) Inner zone of fluid recycle; (II) impeller zone in the range $0 < r < Y$; (III) impeller zone in the range $Y < r < R$.

The torque acting on a differential element of the impeller blade due to the drag force is

$$d\tau = r\, dF = (C_D W \rho_L/2)(2\pi f_S N)^2 r^3\, dr \qquad (48)$$

Such a drag coefficient based approach to power consumption was given by Tatterson (1991). Integrating the above equation between the limits $r = 0-R$ and $\tau = \tau_r-\tau$,

$$\tau - \tau_r = (W\rho_L/8)(2\pi f_S N)^2 (C_D R^4) \qquad (49)$$

Since a power, $P = 2\pi N\tau$,

$$P = \tau_r(2\pi N) + C_D^*(\rho_L W N^3 R^4) \qquad (50)$$

The measured power consumption at $N < N_{CG}$ was correlated using the above equation. It was observed that value of τ_r was zero for single- as well as multiple-impeller systems, and the impeller system could be characterized in terms of the drag coefficient completely.

The above model was extended to include the presence of gas. For this purpose the impeller was divided into three regions. These are the central zone of the liquid recycle, the middle zone of the vortex where gas induction occurs, and the outer zone outside the vortex which conveys the gas (refer to Figure 18). They have made the following additional assumptions: (i) The fluid recycle and the associated effects on the power consumption are assumed to be represented by a constant torque τ_{rg} acting at the eye of the impeller. (ii) For the impeller zone in the range $0 \le r \le Y$, the drag coefficient is C_{DG}. (iii) For the impeller zone in the range $Y \le r \le R$, the drag coefficient is C_{DO}. (iv) The density of the gas−liquid mixture surrounding the impeller is proportional to the liquid density and the square of the radial distance along the impeller blade (i.e., $\rho = A\rho_L(r/R)^2$).

Table 5. Values of Dimensionless Drag Coefficients for Various Multiple-Impeller Systems, Saravanan (1995)

impeller combination	τ_{rg} (N·m)	C_{DO}^*	C_{DY}^*
single PBTD	1.77	22.2	6.7
PBTD−PBTD	0.76	47.9	14.1
PBTD−PBTU	0.39	43.2	13.2
PBTD−SBT	0.79	111.6	27.6
PBTD−DT	0.93	146.5	34.9
PBTD−PD	0.49	9.1	3.0
PBTD−PU	0.15	8.2	2.8

Proceeding in a manner similar to that above, the equation for power consumption is

$$\frac{P - \tau_{rg}(2\pi N)}{\rho_L W N^3 R^4} = C_{DO}^* - C_{DY}^*\left(1 - \frac{1}{\phi_S F}\right)^3 \qquad (51)$$

The above model was also applied by them to the multiple-impeller system. The power consumption for the different impeller combinations could be adequately correlated in terms of the dimensionless drag coefficients. This model has a number of simplifying assumptions such as a constant value of drag coefficients in a particular region and parabolic variation of local density with respect to the radial distance. These assumptions are a simplified picture of reality. Nonetheless, the model helps in characterizing the impeller systems in terms of the drag coefficients. The experiments have been carried out over a large range of vessel sizes (0.57−1.5 m), operating conditions, and impeller geometries. The values of the constants for various impeller combinations have been reported in Table 5. This correlation is expected to be useful in scale-up. It was observed that the value of τ_{rg} is much smaller than the values of C_{DO}^* and C_{DY}^*. They have shown that the power numbers for the multiple-impeller systems decreased in the following order:

PBTD−DT > PBTD−SBT > PBTD−PBTD > PBTD−PBTU > PBTD−PD > PBTD−PU > single PBTD

The design of the lower impellers (PBTD and PBTU) were optimized to reduce the power consumption. It was found that the blade angle of 30° gave the lowest power number. The power number increased with the increasing number of blades and the blade width. The blade thickness did not have a significant effect on the power number. The power number was found to increase with an increase in the interimpeller clearance. The above equation was successfully used in their data for single- as well as multiple-impeller systems within ±10%.

The pertinent literature is reviewed in Table 6. It shows the type of impeller investigated, geometry of the system, physicochemical properties investigated, and the key findings.

3.3.2. Recommendations. As compared to the critical speed and gas-induction rate, studies pertaining to power consumption are not extensive. There is very little information on the power consumption for various designs of gas-inducing impellers; whatever information is there is mainly in the form of empirical correlations. The correlations of Michel and Miller (1962), Arbiter et al. (1969), and Baczkiewicz and Michalski (1988) have not been tested over a wide range and may give erroneous results if applied beyond their range of applicability. Saravanan et al. (1996) have presented

Table 6. Power Consumption in Gas-Inducing Type Contactors

impeller type	geometry	key results	refs
Fagergren	$D = 5-9.4$ cm; $T = 11-20$ cm	$\frac{P_{AL}/P_L - \chi}{1 - P_{AL}/P_L} = \alpha N_Q^n$	Arbiter et al. (1969)
pipe with orifice	$T = 15.8$ cm; $D = 7.5$ cm	$P_G = C(P_L{}^2ND^3/Q_G{}^{0.56})^{0.45}$	Topiwala and Hamer (1974)
Outokumpu (scale-up)	$V = 3$ and 16 m^3; $D = 50$ and 76 cm	$\frac{P_G}{P_L} = \left(\frac{D'}{D}\right)^{7/2} = \left(\frac{L'}{L}\right)^{7/2}$	Fallenius (1981)
Denver Fagergren	$T = 5.11-7.8$ cm	correlated Fr, N_P, Re, and N_Q	Harris and Mensah-Biney (1977)
pipe with orifice	$T = 41-100$ cm; $D = 20-50$ cm	$\frac{P_G}{P_L} = (1 - 17N_Q)$ $P_G = C(P_L{}^2ND^3/Q_G{}^{0.56})^{0.45}$	Joshi and Sharma (1977)
Cassiterite flotation	$V = 6.6$ l	correlated P/V_L as a function of N_Q with N as a parameter	Schubert and Bischoffberger (1978)
turboaerator	$D/T = 0.2$	related P_G as a function of N_{Qg}, C_H, N_P	Zundelevich (1979)
Wemco	$T = 30$ cm; $D = 5$ cm	used (P_G/V_L) to correlate $k_L\underline{a}$, Q_G	Sawant et al. (1980)
Denver	$T = 10-38$ cm; $D = 7-11.5$ cm	used (P_G/V_L) to correlate $k_L\underline{a}$, Q_G	Sawant et al. (1981)
multiple-impeller system	$T = 0.19-0.36$; $D/T = 0.25$	$\frac{P_G}{P_L} = 0.54\left(\frac{N^2D}{g}\right)^{-0.34}\left(\frac{ND^2\rho}{\mu}\right)^{-0.08}$	Matsumura et al. (1982a)
PBTD	$T = 57$ cm; $D = 15-25$ cm	correlated N_{PG}/N_P with V_G using N as a parameter	Raidoo et al. (1987)
hollow pipe	$T = 0.44$ m	$P_G/V_L = 0.6n^{3.4}(Q/V_L)^{-0.3}(d/D)^{4.5}i^{1.1}$	Baczkiewicz and Michalski (1988)
PBTD	$T = 57-150$ cm; $D = 19-50$ cm	modeled P_G based on the forced vortex model	Mundale (1993)
hollow pipe	$T = 0.3$ m; $D = 0.1-0.15$ m	$\frac{Eu_G}{Eu} = 1 - \exp\left(A + \frac{a_1}{\sqrt{Fr^*}} + a_2Re\right)$	Heim et al. (1995)
PBTD−PU	$T = 57-150$ cm; $D = 19-50$ cm	$\frac{P - \tau_{rg}2\pi N}{\rho_L WN^3R^4} = C_{DO}^* - C_{DY}^*\left(1 - \frac{1}{\phi F_S}\right)$	Saravanan et al. (1996)

a simplified model, and their correlation is recommended for scale-up purposes, provided the geometry is not dramatically different.

3.4. Bubble Formation, Gas Holdup, and Interfacial Area. 3.4.1. Type 11, 12, and 22 Systems. The process of bubble formation, gas holdup, and power consumption are intimately related in the case of gas-inducing impellers. Gas induction occurs at $N > N_{CG}$ with a corresponding power consumption. Bubble formation occurs from the induced gas. In the impeller region these bubbles get sheared, causing bubble breakage, and bubbles coalesce in the region of lower stress in the vessel. An equilibrium between the two processes determines the bubble size.

In the conventional mechanically agitated contactors, the fractional gas holdup and the interfacial area depend on the power consumption per unit volume as well as the superficial gas velocity. In the case of gas-inducing impellers, it is not possible to vary the two independently, as beyond N_{CG}, the power consumption and superficial gas velocity are intimately related through the gas-induction process. The power consumption determines the rate of gas induction which in turn influences the gas holdup.

Bubble formation was qualitatively studied by Grainger-Allen (1970). He has used photographic techniques to investigate the cavity formation behind the blades and bubble generation from these cavities. He has studied a variety of slotted, hollow impellers in a small Perspex vessel. He has reported that the presence of stator blades did not influence the bubble size, but it merely increased the number of bubbles generated. The stator blades also helped to modify the flow pattern. Bubble generation was shown to occur from the cavity formed behind the trailing edge of the impeller via the vortex shedding mechanism. The bubble generation occurred only at the tail of the cavity. The presence of a surface-active agent in the liquid phase did not affect the cavity size but merely decreased the bubble size. He further proposed that to improve the bubble formation, energy consumption in the cavity should be increased. This can be carried out by using two impellers in close vicinity of each other, or by suitably perforating the impeller blade to inject the energy into the cavity by a liquid jet.

Hinze (1955) used the theory of bubble breakage due to isotropic turbulence, and assuming that no bubble coalescence takes place, the following equation was derived:

$$d_B = J\left(\frac{\sigma^{0.6}}{\rho_L{}^{0.2}(P_G/V)^{0.4}}\right) \tag{52}$$

Calderbank and Moo-Young (1961) modified this to account for the bubble coalescence by adding a holdup term.

$$d_B = J\left(\frac{\sigma^{0.6}}{\rho_L{}^{0.2}(P_G/V)^{0.4}}\right)\epsilon_G^{\alpha} \tag{53}$$

Both of the above equations show that the mean bubble diameter is inversely proportional to the power consumption per unit volume. The interfacial area ($\underline{a}$) should therefore be proportional to $(P_G/V)^{0.4}$. The correlations of Joshi and Sharma (1977) and Sawant et al. (1981) show that the exponents of (P_G/V) are 0.4 and 0.5, respectively (Table 7). However, Sawant et al. (1980) have reported an exponent of 0.86.

The effect of ionic salts on the gas holdup and interfacial area have been investigated by Joshi and Sharma (1977), Topiwala and Hamer (1974), and Sawant et al. (1980, 1981). They have observed that the electrolytic solutions reduce the bubble coalescence rate and therefore reduce the bubble size and increase the gas holdup. However, this effect diminishes beyond a particular electrolyte concentration.

Table 7. Gas Holdup and Interfacial Area in Gas-Inducing Type Contactors

impeller type	geometry	key results	refs
slotted hollow impellers	$T = 15$ cm; $D = 10$ cm	investigated the bubble generation by photographic techniques	Grainger-Allen (1970)
pipe with orifice	$T = 15.8$ cm; $D = 7.5$ cm	$\epsilon_G \propto (P_G/V_L)^{\beta}(V_G)^{\chi}$	Topiwala and Hamer (1974)
pipe with orifice	$T = 41-100$ cm; $D = 20-50$ cm	$\epsilon_G = 0.00112(P_G/V_L)^{0.5}$ $\underline{a} = A(P_G/V_L)^{0.4}V_G^{\beta}$	Joshi and Sharma (1977)
Wemco	$T = 30$ cm; $D = 5$ cm	$\underline{a} = 79(P_G/V)^{0.86}$ $\underline{a}$ unaffected by solids (dolomite 20% by wt $< 60\ \mu$m)	Sawant et al. (1980)
Denver	$T = 10-38$ cm; $D = 7-11.5$ cm	$\epsilon_G = 0.0325(P_G/V_L)^{0.5}$ $\underline{a} = 75(P_G/V_L)^{0.5}$	Sawant et al. (1981)
multiple-impeller system	$T = 0.19-0.36$ m; $D/T = 0.25$	$\epsilon_G \propto N^2D^{4.1}T^{-2.6}\sigma^{-2.8}\mu^{-0.15}$	Matsumura et al. (1982b)
hollow-bladed concave	$T = 45$ cm; $D = 15.4$ cm	bubble size shows a log normal distribution with $\sigma = 0.31$	Forrester et al. (1994)
hollow pipe	$T = 0.3$ m; $D = 0.1$ m	$\epsilon_G = BFr^{b}Re^{b_2}N_Q^{b_3}(D/S)^{b_4}$	Heim et al. (1995)
Denver	$T = 19$ cm; $D = 9.6$ cm	$\epsilon_G = 10^{-7.8}N^{2.7}Q_G^{0.15}$ $\underline{a} = 0.14N^{0.77}Q_G^{0.28}$	Al Taweel and Cheng (1995)
PBTD with stator multiple impellers	$T = 57-150$ cm; $D = 19-50$ cm	$\epsilon_G = \lambda_1(D/T)^{\lambda_2}(ReFrFl)^{\lambda_3}$	Saravanan and Joshi (1996)
PBTD−stator, multiple impellers with sparging	$T = 1.5$ m; $D = 0.5$ m	$\epsilon_G = \eta_1(ReFrFl)^{\eta_2}(C_3/D)^{\eta_3}$	Patwardhan and Joshi (1997)

Matsumura et al. (1982b) have correlated the fractional gas holdup and the interfacial area in their multiple-impeller system with the gas flow number, the Froude number, and the Reynolds number on the basis of the lower impeller. This is because the lower impeller is designed and operated for the effective dispersion of the induced gas. Hence, it is quite reasonable to assume that the gas dispersion should be dependent on the operating conditions of the lower impeller.

Heim et al. (1995) have investigated hollow pipe impellers with four and six pipes and have given the following correlation for the fractional gas holdup:

$$\epsilon_G = BFr^{b_1}Re^{b_2}N_{QG}{}^{b_3}(D/S)^{b_4} \tag{54}$$

Recently, Saravanan and Joshi (1996) reported the use of multiple impellers in GIMAC for improving the gas-dispersion characteristics. They observed that the gas holdup decreased in the following order:

PBTD−PU > PBTD−PBTU > PBTD−PD > single PBTD > PBTD−PBTD > PBTD−SBT > PBTD−DT

The geometry of the bottom PBTU and PU impeller was further optimized. For this purpose, the blade angle, the number of blades, the blade thickness, and the impeller diameter was varied over a wide range for a PBTU impeller. The fractional gas holdup for a blade angle of 30° was higher than that for blade angles of 45, 60, or 90°. The pumping effectiveness of the impeller was found to decrease with an increase in the number of blades. Thus, increasing the number of blades above six reduced the fractional gas holdup. Further, it was observed that the impeller with four blades gives instabilities in the gas−liquid dispersion. Therefore, they recommend six-bladed impellers. The fractional gas holdup increased with an increasing W/D ratio. The blade thickness did not have a significant effect on the fractional gas holdup. The fractional gas holdup was also found to decrease with an increase in the inter-impeller distance. For a given system geometry, the fractional gas holdup was found to decrease as the solid loading increases. The data on the fractional gas holdup was correlated according to the work of Smith (1991) on stirred vessels. The primary reason for using Smith's correlation was that he was able to correlate the data on fractional gas holdup for a range of stirred vessel sizes and over a wide range of operating conditions. Therefore, it is expected that his correlation should be more scalable. His correlation is given by

$$\epsilon_G = a(D/T)^{b}(ReFrFl)^{c} \tag{55}$$

The above equation correlates the rate of gas supply to the stirred vessel ($Fl = Q_G/ND^3$), the physical properties of the system (Re), and the geometry of the system (Fr), with the fractional gas holdup. The flow number defined here does require information on the gas-induction rate before the gas hold-up can be computed. The factor is introduced because different impellers when operated at the same value of power consumption per unit mass show different gas-induction rates, and hence different gas holdups. The values of a, b, and c for different designs of the lower impeller have been reported in their work. They have reported that the value of "a" varies from 0.06 for a single-impeller system to 1.45 for a PBTD−PBTU combination, whereas the values of "b" are 0.31 and 0.05 for a single-impeller system and a PBTD−PBTU combination, respectively and the value of "c" ranges between 0.51 for a single-impeller system to 0.70 for a PBTD−PBTU system. Since their experiments have been performed over a wide range of vessel sizes (0.57−1.5 m) and a wide range of operating conditions, the correlation is extremely useful for scaleup purposes.

An attempt was also made to correlate the holdup data in terms of power consumption alone. It was found that the data did not correlate well. This is because different impeller configurations give different Q_G and hence ϵ_G at the same value of overall power consumption per unit mass.

Patwardhan and Joshi (1997) have also investigated the fractional gas holdup for GIMAC undergoing simultaneous gas induction and sparging. Their data on fractional gas holdup was also correlated with the above equation. The values of the constants were reported for different designs of the sparger and the lower impeller. However, their experiments were conducted only on 1.5-m vessels and the holdup correlation should be used very carefully.

3.4.2. Recommendations. A preliminary estimate of the gas holdup can be made by using a relation that

Table 8. $k_L\underline{a}$ in Gas-Inducing Type Contactors

impeller type	geometry	key results	refs
pipe with orifice	$T = 15.8$ cm; $D = 7.5$ cm	no clear trend between $k_L\underline{a}$ and d_B. $k_L\underline{a}$ increases with $P_G/\bar{V}$	Topiwala and Hamer (1974)
pipe with orifice	$T = 41-100$ cm; $D = 20-50$ cm	$k_L\underline{a} = A(P_G/V)^{0.55}V_G^B$ $k_L \propto (P_G/V)^{0.15}$	Joshi and Sharma (1977)
Wemco	$T = 30$ cm; $D = 5$ cm	$k_L\underline{a} = 0.0159(P_G/V)^{0.86}$ k_L independent of (P_G/V) $k_L\underline{a}$ increases by 15% due to solids (dolomite 20% by wt, $< 60\ \mu$m)	Sawant et al. (1980)
Denver	$T = 10-38$ cm; $D = 7-11.5$ cm	$k_L\underline{a} = 0.0195(P_G/V)^{0.5}$ k_L independent of (P_G/V)	Sawant et al. (1981)
multiple-impeller system	$T = 0.19-0.36$; $D/T = 0.25$	$k_L = 18.2\left(\frac{\rho}{\mu g}\right)^{-0.33}\left(\frac{\rho D}{\mu}\right)^{0.67}\left(\frac{N^{*3}D^3}{\mu g}\right)^{-0.23}$	Matsumura et al. (1982b)
hollow pipe	$T = 0.44$ m	$k_L\underline{a} = 0.17n^{1.7}(Q/V_L)^{0.6}(d/D)^{2.2}i^{0.5}$	Baczkiewicz and Michalski (1988)
Rushton-type hollow shaft	$T = 7$ cm; $D = 3.2$ cm	$Sh = ARe^{1.45}Sc^{0.5}We^{0.5}$ $A = 3 \times 10^{-4}$ for $H/T = 1$ $A = 1.5 \times 10^{-4}$ for $H/T = 1.4$	Dietrich et al. (1992)
hollow shaft	$T = 5$ cm; $D = 2.9$ cm	$Sh = ARe^{0.44}Sc^{0.5}We^{1.27}$ $A = 0.123$	Hichri et al. (1992)
hollow pipe	$T = 0.3$ m; $D = 0.1-0.15$ m	$\frac{Sh}{Sh_\infty} = 1 - \exp(-KRe^{k_1}Fr^{*k_2})$	Heim et al. (1995)
hollow pipe	$T = 0.45$ m; $D = 0.154$ m	$k_L\underline{a} = 0.01(P_G/V_L)^{0.475}V_G^{0.4}$	Forrester et al. (1998)

correlates the gas holdup empirically to power consumption per unit volume. Such a correlation was given by Joshi and Sharma (1977). The correlation proposed by Smith (1991) is also successful in predicting the holdup in conventional stirred vessels over a wide range of equipment sizes and scale. His correlation was modified and used by Saravanan and Joshi (1996). This correlation is recommended for the estimation of gas holdup in type 22 systems. Gas holdup in type 11 has only been investigated very briefly. It is highly recommended that the gas holdup characteristics of type 11 systems be investigated. The effects of impeller geometry (blade shape, blade angle, number of blades, orifice location, orifice area, etc.) on power consumption and gas holdup should be evaluated. With the help of these data, the optimum geometry for type 11 systems can be established.

4. Performance Characteristics

4.1. Mass-Transfer Coefficient. Many of the gas−liquid reactions involving sparingly soluble gases such as hydrogen, oxygen, and so forth are limited by the transfer of the dissolved gas to the bulk liquid. In such cases, the productivity of the reactor depends on the mass-transfer coefficient. For the design of such systems, the knowledge of the mass-transfer coefficient is of prime importance. Experimentally, the mass-transfer coefficient can be determined by physical or chemical methods.

(i) Physical Methods: This involves absorption of a sparingly soluble gas in the liquid phase under constant volume conditions. During absorption, the pressure of the gas phase decreases, which can be monitored to obtain the volumetric mass-transfer coefficient. Hichri et al. (1992) used this method:

$$\ln\left(\frac{P_O - P_i}{(P - P_i) - k(P_O - P)}\right) = \left[\frac{(k+1)}{k}\right]k_L\underline{a}t \quad (56)$$

(ii) Chemical Methods: This involves simultaneous absorption and reaction of a solute gas into the liquid phase. Several systems are reported in the literature for the measurement of $\underline{a}$ and $k_L\underline{a}$ (Doraiswamy and Sharma, 1984). The absorption of lean carbon dioxide in an aqueous solution of sodium carbonate and sodium bicarbonate can be used to determine the liquid-side mass-transfer coefficient, $k_L\underline{a}$. Absorption of oxygen from air into an aqueous solution of sodium hydrosulfite can be used to determine the effective interfacial area, $\underline{a}$. In any case, when the gas phase is not pure, the residence time distribution of the gas phase plays an important role in the analysis of the data. The value of $k_L\underline{a}$ can be calculated by assuming a certain residence time distribution of the gas phase (plug flow or back-mixed). An assumption of a back-mixed gas phase leads to much higher values of $k_L\underline{a}$ as compared to those from the assumption of plug flow. The difference in the two values of $k_L\underline{a}$ increases as the gas-phase conversion approaches unity. In general, the error between the two values is small at gas-phase conversions less than 10%. Thus, in such studies, it is usually desirable to limit the gas-phase conversion to below 10%. Table 8 summarizes the various efforts made at investigating the mass-transfer coefficient ($k_L\underline{a}$). The correlations are empirical and correlate the $k_L\underline{a}$ value with either power consumption per unit mass or the dimensionless numbers such as *Re*, *Fr*, *We*, and so forth.

From Tables 7 and 8 it is also possible to see the variation in k_L with the power consumption. Joshi and Sharma (1977) have found the liquid-side mass-transfer coefficient (k_L) to be proportional to the power input ($k_L \propto (P_G/V)^{0.15}$); thus k_L depends only on the power consumption per unit volume. This is because the power input per unit volume governs the superficial gas velocity through the induction process. The energy dissipation rate alone governs the turbulence structure, and hence the value of k_L depends only on the power input per unit volume. It may be noted that the value of the exponent is small. Sawant et al. (1980, 1981) found k_L to be independent of the power consumption per unit volume.

4.2. Solid Suspension. Solid suspension is of great practical importance in froth flotation as well as in many of the gas−liquid operations. Suspension of the particles is important to ensure good gas−liquid−solid contact. Ore enrichment in froth flotation occurs because of efficient gas−liquid−solid contact. In certain gas−liquid reactions the solid particles act as catalysts; therefore, a uniform solid suspension is necessary for

making the entire reactor volume effective. Although the solid suspension is of prime importance, this aspect has received scant attention. Only Saravanan et al. (1997) have investigated the solid suspension in GIMAC in detail.

They have reported that a single gas-inducing impeller is very poor for the suspension of solid particles. If the gas-inducing impeller is kept close to the liquid surface, the flow and turbulence near the bottom of the tank becomes feeble, causing very little solid suspension. Even when the gas-inducing impeller was located close to the bottom, solid suspension was found to be possible only when the particle size is less than 100 μm and solid loading less than 1%. The gas-induction rate in this case was extremely low. However, a multiple-impeller system was found to be more effective for a solid suspension. In this case, the second impeller can be located well-below the gas-inducing impeller. The flow and the turbulence near the tank bottom can be increased substantially, resulting in better solid suspension. The critical impeller speed for solid suspension (N_{CS}) was measured for different impeller systems, under a wide range of operating conditions. It was observed that N_{CS} increased in the following order:

$$\text{PBTD}-\text{PBTD} < \text{PBTD}-\text{SBT} < \text{PBTD}-\text{DT} < \text{PBTD}-\text{PBTU} < \text{PBTD}-\text{PU}$$

This was explained on the basis of the axial velocity generated by the different bottom impellers. A PBTD impeller generates an axial flow in the downward direction and is therefore most efficient for the process of solid suspension. SBT and DT, however, are radial flow impellers; as a result, only a small portion of the input energy dissipated is utilized for the solid suspension. PBTU and PU generate an axial flow in the upward direction and therefore even smaller amount of input energy is available for solid suspension. In this case also the interimpeller clearance was found to be an important parameter. The critical impeller speed for solid suspension, N_{CS}, decreases with an increase in the interimpeller clearance.

On the basis of the above results, the geometry of the bottom PBTD impeller was optimized. They have recommend a 45°, six-bladed pitched blade downflow turbine with a W/D ratio of 0.3 for efficient solid suspension. The blade thickness did not have any significant effect on N_{CS}. The value of N_{CS} was found to decrease with an increase in the impeller diameter. It decreases with a decrease in the terminal settling velocity of particle and solid loading. N_{CS} decreases with a decrease in the impeller clearance from the bottom. N_{CS} also decreases with an increase in the interimpeller clearance. It is unaffected by the submergence of the upper impeller. They have also proposed a model for the solid suspension on the basis of the mechanism of the fluidization of solid particles, and the liquid circulation velocities generated by the impeller. They have developed the following correlation:

$$N_{CS} = 0.031\left(\frac{\rho_S - \rho_L}{\rho_L}\right)A^{-0.83}(W/D)^{-0.314}d_p{}^{0.17}X^{0.15} \times (C_3/D)^{-0.446}D^{-2.42}(C_1/T)^{0.127}T^{1.35} \quad (57)$$

The constant 0.031 has the following units ($m^{1.072}\cdot rad^{0.83}\cdot\mu m^{-0.17}\cdot s^{-1}$). Since the above correlation was developed for a large range of vessel sizes (0.57−1.5 m) and under a wide range of operating conditions, it is expected to be very useful for scale-up purposes. The above correlation also compares favorably with the classical Zwietering correlation for stirred vessels.

5. Process Design of Gas-Inducing Reactors

The objective of a process design engineer can be simply stated as "design a reactor that will give a certain production rate". More specifically, the process design engineer has to determine the set of parameters that will ensure the desired production rate (throughput), such that the overall operation becomes economically viable and attractive.

The correlations recommended in sections 3 and 4 are based on the experimental work carried out by Saravanan and Joshi (1995, 1996) and Saravanan et al. (1996, 1997). These experiments have been carried out over a wide range of variables such as locations of the impellers, interimpeller spacing, impeller designs, vessel sizes, power consumption, and so forth. Therefore, the correlations developed from these studies would be valid on a larger scale even when any similarity (geometric, constant tip speed, constant power consumption per unit volume, etc.) is not maintained. Since a wide range of design variables has been covered for developing correlations, the only uncertainty is concerned with the differences associated with the gas−liquid and gas−liquid−solid systems. The extent of uncertainty can be considerably reduced by performing a few experiments with the actual system (gas, liquid, and solid) at the corresponding temperatures and pressures and then use the correlations recommended in this monograph. These correlations are useful in the estimation of design parameters such as the rate of gas induction, fractional gas hold-up, power consumption, critical impeller speed for solid suspension, and so forth.

Before applying these correlations, it is important to know which of the above design parameters is important. Thus, the first step in the process design activity is the determination of the rate-controlling mechanism. A particular equipment geometry (reactor size) and operating conditions (power consumption) are chosen. The power consumption level is chosen such that the reactor gives the desired throughput. These steps are repeated for several different values of the reactor size. This finally yields a set of reactor sizes and the corresponding operating conditions at which the reactor is able to give the desired throughput. An economic analysis is then carried out to determine the optimum reactor geometry and the corresponding operating conditions.

5.1. Determination of the Rate-Controlling Step. A typical reaction between a gas and a liquid (catalyzed by solid particles) involves many steps (diffusion through the gas film, diffusion through the liquid film, adsorption on the catalyst-active sites, surface reaction, desorption of the products, etc.). It is customary to denote the gas-phase reactant by A, and the liquid-phase reactant as B. These steps involved are shown schematically in Figure 19. Any one of the above steps may be a rate-determining step. In addition, if the reaction is highly endothermic or exothermic (typical of oxidation and hydrogenation reactions), then heat has to be supplied or removed from the reactor. In certain cases it is possible that this rate of heat supply or removal may control the overall rate of the reaction. In gas−liquid reactions catalyzed by solid particles, it is also

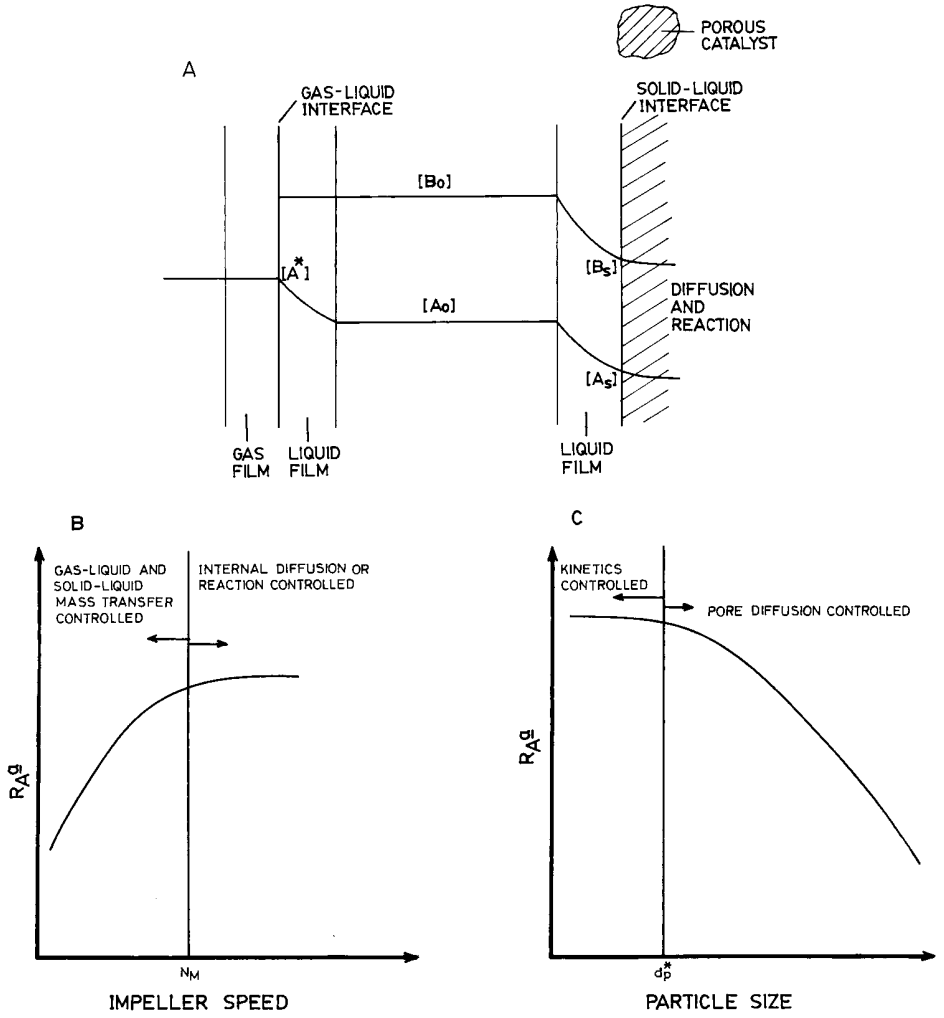

Figure 19. (A) Various steps involved in gas−liquid−solid reaction.

Table 9. Effect of Various Parameters on the Overall Rate of Reaction

	effect of increase in the variable on the overall rate of reaction							
rate-controlling step	[A*]	$[A_O]$	$[A_S]$	$[B_O]$	$[B_S]$	ϵ_S	d_P	N
gas−liquid mass transfer	$\propto$[A*]	$\propto\{[A^*] - [A_O]\}$	$[A_S] = [A_O]$	no effect	no effect	no effect	no effect	increases
solid−liquid mass transfer	$[A^*] = [A_O]$	$\propto[A_O]$	$\propto\{[A_O] - [A_S]\}$	no effect	no effect	$\propto\epsilon_S$	$\propto\{1/d_P\}$	increases
pore diffusion	$[A^*] = [A_S]$	$[A_O] = [A_S]$	$\propto[A_S]$	no effect	no effect	no effect	$\propto\{1/d_P\}$	no effect
chemical reaction	$[A^*] = [A_S]$	$[A_O] = [A_S]$	$\propto[A_S]^m$	$[B_O] = [B_S]$	$\propto[B_S]^n$	$\propto\epsilon_S$	no effect	no effect

possible that the suspension of catalyst particles can determine the overall rate of reaction. In such cases the overall reaction is said to be suspension-controlled. As a first step in the process design activity, the rate-controlling step has to be determined. The determination of the rate-controlling step is usually carried out using model contactors. This procedure is fairly well-established (Doraiswamy and Sharma, 1984). Table 9 summarizes the effect of various parameters such as [A*], $[A_S]$, $[B_O]$, d_P, ϵ_S, impeller speed, and so forth, on the overall rate of reaction for different rate-controlling steps. During the course of the reaction, it may happen that one or more operating conditions change. For example, the reactant concentration, operating temperature, pressure, and so forth may change with time (batch reactor) or location within the reactor (packed column). In that case, it is possible that the rate-controlling step itself may change with time or location in the vessel. In such cases, the rate-controlling step has to be determined as a function of time/location in the reactor, and so forth. Once the rate-controlling step is known, the overall rate of reaction can be written. This overall rate of reaction can then be integrated with respect to space, or time, to determine the throughput of the reactor.

5.2. Optimization of the Geometry for the Desired Design Objectives. It is clear from the discussion in sections 3 and 4 that the performance of the multiple-impeller system is superior as compared to a single gas-inducing impeller. This is mainly because, in such a system, the upper gas-inducing impeller can be kept close to the liquid surface (about 100−200 mm below the liquid surface, irrespective of the scale of operation) for achieving high rates of gas induction. For performing other duties like gas dispersion (distribution of the induced gas throughout the equipment), solid suspension, heat transfer, mixing, and so forth, the second impeller can used. The design of the lower impeller can be optimized for different duties such as high fractional gas holdup, good solid suspension ability,

Table 10. Recommendations for Different Design Objectives

design objective	recommended design of lower impeller	reasons
dispersion/mass transfer	upflow impeller at the bottom along with a large ring sparger	Upflow impeller helps in gas dispersion by creating a favorable flow pattern. Sparger introduces additional gas in the system which increases the throughput.
suspension	downflow impeller at the bottom	This results in generating large liquid velocities near the vessel bottom. This aids the solid suspension process. Better solid suspension can be achieved at same power consumption.
heat transfer	upflow impeller at the bottom, cooling coils, jacket depending on the need	The upflow impeller at the bottom generates gross (top to bottom) liquid circulation, which helps in keeping the vessel contents well-mixed and ensures good values of the heat-transfer coefficient.

and so forth (Saravanan and Joshi, 1995, 1996) and Saravanan et al. (1996, 1997). This activity has clearly shown that the optimum design of lower impeller changes with the design objective. For example, to achieve high fractional gas holdup, it is desirable to use an upflow impeller at the bottom, whereas to achieve good solid suspension, a downflow impeller at the bottom is desirable. It is recommended that such a multiple-impeller system be used for commercial scale equipment. The recommended lower impeller designs for different design objectives such as gas dispersion, solid suspension, heat transfer, and so forth along with the reasons are summarized in Table 10.

The procedure for process design will now be illustrated with the help of a case study. It is assumed that the reaction is characteristic of hydrogenation of a typical organic compound. The gas- and liquid-phase reactants are denoted by A and B, respectively. For the purpose of illustration it will be assumed that the overall reaction is mass-transfer-controlled. It is desirable to carry out such a reaction in a gas-inducing contactor along with a sparger (Patwardhan and Joshi, 1997). The lower impeller will be considered as a PBTU (pitched blade upflow turbine) and a large-size ring sparger will be assumed. Let V_{Gi} be the superficial velocity of the sparged gas. A part of this sparged gas reacts in the vessel and the remainder escapes into the headspace. Simultaneously, the gas is recycled back into the liquid with the help of a gas-inducing impeller. A part of the entrained/induced gas also reacts, and the remainder escapes into the headspace. If overall material balance is taken for the entire vessel, then the maximum permissible value of the superficial gas velocity (V_{Gi}) should be such that the rate of gas sparging equals the rate of reaction of the gas in the vessel. This ensures that the headspace pressure will neither rise nor fall with time. Alternatively, if the overall material balance is written for the headspace, then it is clear that the net rate of escape of the unreacted gas into the headspace (Q_{UG}) must be equal to the rate of gas induction.

Figure 20A shows the comparison of fractional gas holdup under sparging conditions, with and without the use of a gas-inducing impeller. In the absence of a gas-inducing impeller such a system behaves like a conventional mechanically agitated contactor (MAC). The comparison is made in terms of gas holdup as a function of power consumption per unit volume for different superficial velocities of sparged gas (V_{Gi} = 0, 6, 18, and 29 mm/s). From the figure it can be seen that the fractional gas holdup in the presence of a gas-inducing impeller is substantially higher as compared to that of a MAC. Similarly V_{Gi} = 0 corresponds to the case of gas induction alone (no sparging). It can also be seen that as the rate of sparging increases, the gas holdup

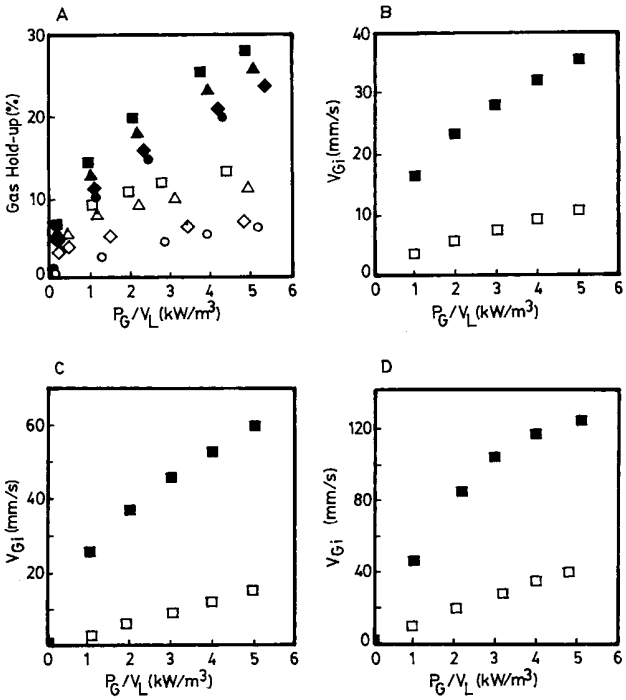

Figure 20. Comparison of MAC with and without a gas-inducing impeller (open symbols, without a gas-inducing impeller; filled symbols, in the presence of a gas-inducing impeller). For the calculations the following correlations were used. N_{CG} in the absence of sparging: $N_{CG} = [1/2\pi R]\sqrt{(2gS)/\phi}$. change in N_{CG} due to sparging: $[(\Delta N_{CG})^2\pi^2 D^2\phi]/[2gS] = \alpha_1(C_3/D)^{\alpha_2} V_G^{\alpha_3}(S/T)^{\alpha_4}$. gas-induction rate in the absence of sparging: $Q_G = \lambda^* N R^2(1 - [2gS]/[\phi V^2] + \alpha^* N R^3(1 - A([2gS]/[\phi V^2])^{3/2})$. change in the gas-induction rate due to sparging: $1 - Q_{GS}/Q_G = \beta_1 Fl^{\beta_2}(C_3/D)^{\beta_3}$. fractional gas holdup: $\epsilon_G = a(D/T)^b(ReFrFl)^c$. power consumption: $P_G/P_O = 0.1\text{-}([NV_1]/Q_G)^{1/4}([N^2D^4]/[WV_L^{2/3}g])^{-1/5}$, $P_O = N_P\rho_L N^3 D^5$. (A) the rate of gas induction as a function of the power consumption with the superficial gas velocity as a parameter: ○, 0 mm/s; ◇, 6 mm/s; △, 18 mm/s; □, 29 mm/s. (B) Mass-transfer controlled. (C) Enhancement in the rate of mass transfer due to chemical reaction, $\sqrt{M}$ = 5. (D) Enhancement in the rate of mass transfer due to chemical reaction, $\sqrt{M}$ = 50. For parts B−D of the reaction it was assumed that the production rate was 50 ton/day of compound R by the following reaction: $3A_{(g)} + B_{(l)} \rightarrow R_{(l)}$. The solubility of A in a liquid was assumed to be equal to [A*] = 0.1 kmol/m^3. It was assumed that the reaction takes place at 150 °C and at 10 atm of pressure. The estimation of the performance was carried out with the correlations given above. In addition, the following correlations were used. Mean bubble diameter: $d_B = 4.15([(P_G/V_L)^{0.4}\rho_L^{0.2}]/\sigma^{0.6}])^{-1}\epsilon_G^{0.5} + 0.09$. Interfacial area per unit volume: $\underline{a} = 6\epsilon_G/d_B$. The volumetric mass-transfer coefficient as $k_1\underline{a} = 0.00\overline{2}\underline{a}$.

increases. The following stepwise procedure is recommended for design:

(a) The stoichiometry of the reaction under consideration is known. Further, the solubility of gas and the physicochemical properties of the gas and the liquid phases were assumed to be available.

(b) The geometry of the system is first chosen (e.g., the tank diameter, impeller design, D/T ratio, clearance, submergence, sparger size, impeller speed, etc.). These are chosen on the basis of the rate-controlling step and recommendations in Table 10.

(c) A particular superficial gas velocity is chosen V_{Gi}.

(d) For this value of superficial gas velocity, the gas-induction rate (Q_G), fractional gas holdup (ϵ_G), and power consumption (P_G) are calculated both in the presence of a gas-inducing impeller and in the absence of a gas-inducing impeller. For estimation of these hydrodynamic characteristics, the recommended correlations are used.

(e) On the basis of these hydrodynamic characteristics the volumetric mass-transfer coefficient ($k_L\underline{a}$) is calculated. Alternatively, the value of $k_L\underline{a}$ could also be measured in a small-scale experimental reactor (at least larger than 0.5 m in diameter) under the actual conditions prevailing (temperature, pressure, physicochemical properties, etc.)

(f) From the value of $k_L\underline{a}$ the rate at which the sparged and the induced gas react is estimated.

(g) The net rate at which the sparged gas accumulates (Q_{UG}) into the headspace is calculated as the difference between the rate of sparging and the rate of reaction of the sparged gas.

(h) If the Q_G is lower than Q_{UG}, pressure builds up in the headspace and V_{Gi} is unacceptable, or if Q_G is higher than Q_{UG}, headspace pressure decreases and again V_{Gi} is unacceptable. Thus, a new value of V_{Gi} is chosen and the procedure is repeated from step (c) onward until $Q_{UG} = Q_G$. Thus, this procedure yields a value of acceptable V_{Gi} for a given geometry of the system (step b).

(i) The whole procedure is repeated by choosing different operating conditions such as the impeller speed so that different values of $V_{Gi} - P_G$ are generated.

(j) The entire procedure can be repeated if there is an enhancement in the rate of mass transfer due to a chemical reaction. The results of the above procedure are given in Figure 20, parts B−D.

Figure 20B shows that, for a particular value of power consumption per unit volume, a higher value of V_{Gi} is permissible when a gas-inducing impeller is used along with a sparger. For example, for a power consumption of 2 kW/m^3 the permissible V_{Gi} is about 23 mm/s when a gas-inducing impeller is used as compared to about 6 mm/s when the gas-inducing impeller is not present. A higher permissible V_{Gi} in the existing equipment implies that higher productivity can be realized when a gas-inducing impeller is used along with a sparger. If the productivity is to be kept the same, then a higher permissible V_{Gi} implies that a smaller size of the reactor can be used. If the reaction being carried out involves highly corrosive chemicals (hydrogenation of chloro compounds), then an exotic material of construction has to be used (hastalloy, titanium, tantalum, etc.). A reduction in size of such a reactor implies a considerable savings in the equipment cost. Alternatively, if the permissible V_{Gi} is to be kept the same (corresponding to the desired rate of production), then a much smaller power consumption is required when the gas-inducing impeller is employed. That is, for a V_{Gi} of 10 mm/s, 5 kW/m^3 are required when a gas-inducing impeller is not used as compared to about 0.5 kW/m^3 when a gas-inducing impeller is used. A lower power consumption results in a significant reduction in operating costs. This is particularly important when the cost of electricity is very high. A comparison of Figure 20, parts B−D, reveal that the difference in V_{Gi}, or power consumption, increases as the enhancement factor increases.

From the above discussion it is clear that a given rate of production can be achieved by different combinations of the reactor size and the level of power consumption. The selection of the optimum reactor size is based on the annualized cost of the reactor. The annualized cost consists of the cost of capital (depreciation and interest on fixed cost) and the operating cost. The fixed cost consists of mainly the equipment cost, that is, the material cost plus fabrication cost; the operating cost consists mainly of electricity (power) cost. For the purpose of this illustration, five different materials of construction were selected having costs 0.3, 1.0, 3.0, 10.0, 30.0 \$/kg. This range of cost covers practically all the materials commonly used in industry, such as mild steel, stainless steel, glass-lined, hastalloy, titanium-lined vessels, and so forth. Two levels of (depreciation + interest) have been examined: 20% and 50% per year. Three different values of the cost of electricity have been taken: 0.035, 0.10, and 0.30 \$/kW·h.

For a particular reactor volume and the operating pressure, the thickness of the shell and dished ends were calculated. Knowing the density of the material, the weight of the shell was estimated. An extra amount, 50%, was added for the nozzles, supports, shaft, impellers, agitator drive, and so forth. In addition, the fabrication cost was considered 60% of the material cost. The operating cost was calculated as the product of power consumption and the electricity cost. The annualized costs is the sum of the cost of capital and the operating cost. The selection of the optimum reactor size can be made on the basis of the annualized cost. It can be appreciated that the numbers selected, though provisional, do not matter as far as the objective of the exercise is concerned. Because, in reality, any combination of material and fabrication cost and the rate of depreciation and interest will most probably fall in the range considered here. For convenience, Figure 21, parts A−D, indicate the total cost of fabricated equipment per kilogram per year.

Figure 21A shows the annualized cost with the electricity cost of 0.035 \$/kW·h and the cost of capital at 20% per year. Several conclusions can be drawn from this figure. For low-cost materials such as mild steel, the annualized cost decreases as the reactor volume is increased. This is because the fixed cost is low and the operating cost contributes significantly to the annualized cost. Thus, choosing a larger reactor volume and consequently keeping a lower level of power consumption reduces the annualized cost. For medium cost materials (10 \$/kg), there is a certain reactor size at which the annualized cost is minimum. If the reactor size is larger than this value, then the fixed cost increases more than the decrease in power consumption. Whereas if the reactor volume is lower than the optimum value, then the operating cost increases more than the decrease in the fixed cost. This optimum reactor size is shifted to lower volumes as the cost of the material increases. That is, if the material cost is 10 \$/kg, then the optimum reactor size is about 4 m^3, and if the material cost is 30 \$/kg, then the optimum reactor size is about 2 m^3. Thus, for any value of the material cost and the electricity cost, the annualized cost can be calculated and the optimum size of the reactor can be found.

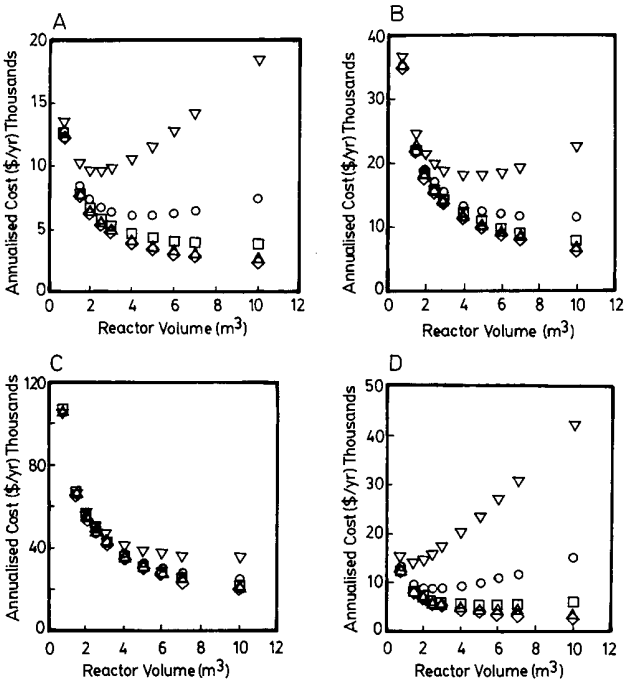

Figure 21. Effect of material cost on the annualized cost (reaction conditions and correlations used are the same as those in Figure 20). (A) Cost of capital = 20%; electricity cost = 0.035 $/kW·h: ◇, 0.144 $/kg·yr; △, 0.48 $/kg·yr; □, 1.44 $/kg·yr; ○, 4.8 $/kg·yr; ▽, 14.4 $/kg·yr. (B) Cost of capital = 20%; electricity cost = 0.10 $/kW·h: ◇, 0.144 $/kg·yr; △, 0.48 $/kg·yr; □, 1.44 $/kg·yr; ○, 4.8 $/kg·yr; ▽, 14.4 $/kg·yr. (C) Cost of capital = 20%; electricity cost = 0.30 $/kW·h: ◇, 0.144 $/kg·yr; △, 0.48 $/kg·yr; □, 1.44 $/kg·yr; ○, 4.8 $/kg·yr; ▽, 14.4 $/kg·yr. (D) Cost of capital = 50%; electricity cost = 0.035 $/kW·h: ◇, 0.36 $/kg·yr; △, 1.2 $/kg·yr; □, 3.6 $/kg·yr; ○, 12.0 $/kg·yr; ▽, 36.0 $/kg·yr.

A comparison of Figure 21, parts A, B, and C (electricity cost 0.035, 0.10, and 0.30 $/kW·h), reveals that the optimum reactor size shifts toward higher volumes. Thus, as the cost of electricity rises, it is preferable to use large reactors and decrease the power consumption to reduce the operating costs. A comparison of Figures 21, parts A and D, shows that as the cost of capital increases (from 20% to 50%), the optimum reactor size shifts to lower values. This shows the advantage of a smaller reactor size to keep the fixed cost low, even though the power consumption (operating costs) increases.

5.3. Design of Impellers for Froth Flotation. 5.3.1. Determination of the Rate-Controlling Step. As with the design of gas−liquid−solid reactors, the design of flotation cells involves the determination of the rate-controlling step. For this purpose, it is necessary to carry out laboratory experiments. The kinetics of flotation are usually represented with a power law model ($dC/dt = k_1C^n$). The laboratory experiments should be carried out to determine the values of k_1 and n. The schematic diagram of a experimental setup that can be conveniently used to carry out these experiments is shown in Figure 22. These experiments should be carried out on at least a 0.5-m diameter scale so that the results can be scaled up with a fair degree of confidence. The gas-inducing impeller should be located sufficiently away from the layer of settled solids, so that it does not play any role in the solid suspension process. That is, the gas-inducing impeller alone should be incapable of suspending the solid particles. The exact location of the gas-inducing impeller may vary with the particle size, loading, and so forth and can be determined from some preliminary runs. Since the submergence is high, the rate of gas induction is low and an arrangement should be provided to supply additional gas at a known and controlled flow rate to the gas-inducing impeller. A second impeller should be used near the settled layer of solids (downflow turbine type). It is desirable to place this impeller on a separate shaft. The advantage of this is that its speed can be controlled independent of the speed of the gas-inducing impeller. The speed of this lower impeller can be changed to get solid suspension to any desired extent. This allows a control over the gas dispersion and solid suspension independent of each other. In principle, the system described is similar to that used by Matsumura et al. (1982a).

In the first set of experiments, the effect of interfacial area, bubble size, and bubble-size distribution on the flotation rate can be investigated. For this purpose, the air flow rate, speed of the gas-inducing impeller, and the geometry of the stator can be varied. In all these experiments, it is necessary to change the speed of the lower impeller to keep the extent of solid suspension at the same level. In each experiment, the rate of flotation, the interfacial area, mean bubble size, and bubble-size distribution should be measured. The effect of these parameters on k_1 and n can then be quantified.

In the second set of experiments, the effect of solid suspension on the flotation rate can be investigated. To achieve this, the lower impeller speed and diameter can be varied. It is well-known that as the impeller speed increases, the solids slowly start getting suspended and the interface between the suspended solids and the clear liquid moves upward. The impeller speed can be adjusted to get any desired value of L_S (Figure 22). When the lower impeller speed is changed, it may in turn affect the dispersion of gas. This effect on gas dispersion can be minimized by adjusting the gas flow rate and the speed of the gas-inducing impeller. This set of experiments can establish the relation between the flotation rate (in terms of k_1 and n) and the extent of solid suspension (L_S).

A third set of experiments needs to be carried out to investigate the effects of additives and their concentration on the flotation rate. These three sets of experiments help to identify the rate-controlling step. This completes the first step in the overall process design activity.

5.3.2. Optimization of the Geometry for the Desired Design Objectives. The next step in the process design involves choosing a system geometry and operating conditions. Since the depth of the froth separation zone is an important parameter, it is desirable to keep constant submergence as the scale of operation increases (Flint (1973), Harris (1986)). Also, for solid suspension purposes, the impeller clearance from the bottom should be kept low. This limits the overall liquid depth in the flotation cell. This means that as the volume increases, the characteristic length of the flotation cell increases like the square root of the volume ($L_C \propto V_L^{0.5}$). This criterion has been reported in much of the literature on flotation. For very large capacities, the characteristic length (L_C) may become very large. In that case, the whole operation may be split up into a battery of small cells operated in series/parallel mode.

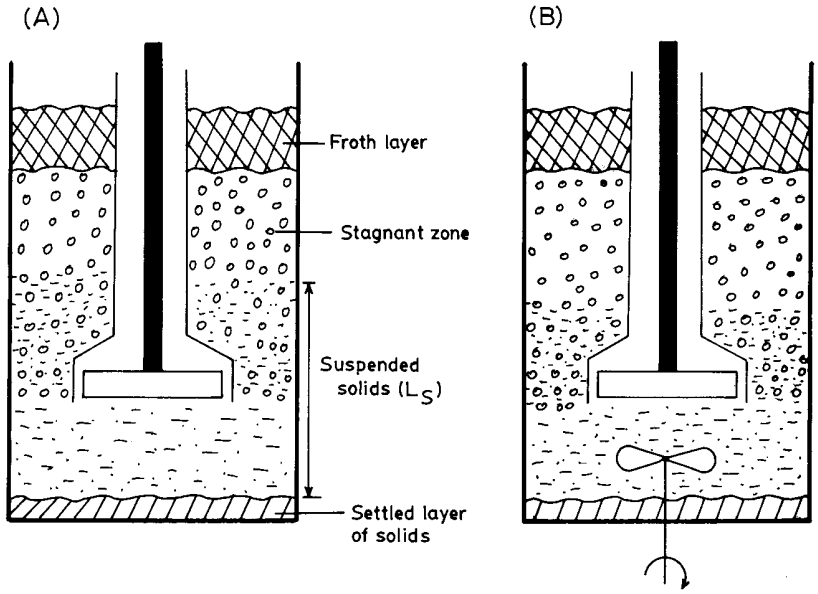

Figure 22. Schematic diagram of the setup in which experiments should be carried out to determine the rate-controlling step.

If the flotation operation is dominated by the dispersion of gas bubbles, then a high shear gas-inducing impeller should be used. This can be a stator−rotor assembly (Denver, Wemco designs, or the design reported by Saravanan et al. (1994)) having a small clearance between them. This will enable the generation of small bubbles of uniform size. If the suspension of solids and contact between gas and solids is important, then it is recommended to use a second impeller below the gas-inducing impeller which enables efficient solid suspension.

6. Conclusions

(1) The various designs of gas-inducing impellers and flotation cells reported in the literature have been classified into three types, depending on the flow characteristics in the impeller zone.

(2) The critical impeller speed for gas induction, N_{CG}, is reached when the velocity head generated by the impeller is sufficient to overcome the hydrostatic head above the impeller. Impeller submergence is therefore a major parameter that influences the overall performance.

(3) In a type 11 system, the gas-induction rate can be estimated by considering the pressure differential generated by the impeller and various resistances to the flow of gas through the impeller. For type 22 systems, Saravanan et al. (1994) and Saravanan and Joshi (1995) have presented a model based on the processes of bubble entrapment and bubble carriage. The multiple-impeller system reported by Saravanan and Joshi (1995) gives a much higher gas-induction rate as compared to other designs reported in the literature.

(4) The gas holdup, mass-transfer, mixing, and heat-transfer characteristics of gas-inducing impellers have not been studied exhaustively. The multiple-impeller system reported by Saravanan et al. (1996, 1997) is recommended because it allows flexibility of design of the lower impeller for achieving a certain design objective, and at the same time maintains a gas-induction rate at a high value.

(5) A process design algorithm has been presented for the design of gas-inducing impellers. Guidelines have also been given about the selection of geometry for different design objectives such as dispersion, mass transfer, heat transfer, solid suspension, mixing, and so forth. Recommendations have been made regarding the correlations to be used for the estimation of the performance of gas-inducing impellers. The process design algorithm has been illustrated for a case study. It has been shown that the use of a gas-inducing impeller in a conventional stirred vessel can lead to a substantial increase in the productivity. The optimum vessel size may not correspond to maintaining constant power consumption, equal tip speed, and so forth on scale-up.

7. Suggestions for Future Work

(1) Since the local pressure plays an important role, further work is needed to establish the relation between impeller design and the local pressure. Such an exercise will help in the rational design and optimization of all types of gas-inducing impellers. Likewise, the relationship between the local pressure and the rate of gas induction needs to be established for type 12 and 22 systems.

(2) It is highly recommended that the future experimental investigations be carried out using larger sized vessels ($T > 0.5$ m) and over a larger range of operating conditions. Systematic investigations have to be carried out to quantify the effects of impeller design and the operating conditions on the performance characteristics such as mixing, mass transfer, interfacial area, heat transfer, and so forth. The effects of physical properties on the hydrodynamic characteristics have been investigated only over a limited range by a few workers. Further work is required in this area.

(3) To be able to design these reactors on fundamental principles, the relation between the impeller−vessel geometry, the flow and pressure field generated, and the design objective such as homogenization, power consumption, gas dispersion, mass-transfer coefficient, solid suspension ability, and so forth has to be established. Recent developments in experimental techniques such as laser Doppler velocimetry (LDV) and

computational tools such as computational fluid dynamics (CFD) should be used to address these issue.

Acknowledgment

The authors would like to acknowledge the experimental work carried out by K. Saravanan and V. D. Mundale. This work has established optimum designs of impellers for achieving different design objectives. On the basis of this work guidelines have been given for the selection of impeller geometries.

Nomenclature

A = constant in eq 41
$[A^*]$ = solubility of the gas in a liquid, kmol/m^3
$[A_O]$ = concentration of the solute gas in a bulk liquid, kmol/m^3
$[A_S]$ = concentration of the solute gas at the solid−liquid interface, kmol/m^3
A_o = orifice area, m^2
$\underline{a}$ = gas−liquid interfacial area, m^2/m^3
$\underline{a}_P$ = solid−liquid interfacial area, m^2/m^3
$[B_O]$ = concentration of the reactant in the bulk liquid phase, kmol/m^3
$[B_S]$ = concentration of the reactant at the solid−liquid interface, kmol/m^3
C_O = orifice discharge coefficient
C_1 = impeller clearance from bottom, m
C_3 = interimpeller clearance, m
C = constant in eq 9
C_D = drag coefficient
C_{DG} = drag coefficient in the zone $0 < r < Y$
C_{DO} = drag coefficient in the zone $Y < r < R$
C_D* = scaled drag coefficient
C_{DO}* = scaled drag coefficient
C_{DY}* = scaled drag coefficient
C_H = impeller head coefficient in eq 28
$C_P(\theta)$ = pressure coefficient
c, c_1, c_2 = constants in eq 27
D = impeller diameter, m
DT = dist turbine
D_O = diffusivity of solute gas, m^2/s
d = diameter of pipe, m
d_B = mean bubble size in gas−liquid dispersion, m
d_P = mean particle size, m
EJLR = ejector jet loop reactor
Eu = gas-phase Euler number
F = constant in eq 51, $2gS/\phi V^2$
f_m = conformity or slip factor
Fl = flow number
Fr = Froude number based on submergence, N^2D^2/gS
Fr_C = Froude number at critical speed, $N_{CG}2D^2/gS$
G = molar absorption rate, kmol/s
g = gravitational acceleration, m/s^2
g_e = molar flow rate of entrained gas escaping back into headspace, kmol/s
g_i = molar flow rate of surface-entrained gas, kmol/s
GIC = gas-inducing contactor
H = total liquid height, m
H_O = solubility coefficient of a solute gas, kmol/MPa·m^3
h_L = liquid head outside the orifice, m
h_S = liquid head above the orifice in absence of gas flow, m
J_O = specific absorption rate of solute gas, kmol/m^3·s
K = slip between impeller and fluid
K_1 = constant in eq 18
k = head reduction coefficient, eq 28
k_1, k_2 = first- and second-order rate constants, 1/s and m^3/s·kmol, respectively
$k_{2,0}$ = second-order rate constant, m^3/s·kmol
k_g = constant in eq 39
k_{mn} = rate constant for the reaction, m$^{3(m+n-1)}$/kmol$^{(m+n-1)}$·s
k_L = liquid-side mass-transfer coefficient, m/s
L_C = characteristic length of the flotation cell, m
L_S = characteristic length of the layer of suspended solids, m
m = order of reaction with respect to the dissolved gas concentration
MAC = mechanically agitated contactor
n = order of reaction with respect to the concentration of the reactant in the liquid phase
N = impeller rotational speed, rps
N_{CG} = critical impeller speed for gas induction, rps
N_{CS} = critical impeller speed for solid Suspension, rps
N_P = power number
N_{QG} = gas flow number
ΔN_{CG} = N_{CG} with sparging − N_{CG} without sparging, rps
n_P = number of pipes
P = pressure, N/m^2
P' = dimensionless pressure
P_G = power drawn by gassed impeller, W
P_H = holding tank pressure, N/m^2
P_{HS} = headspace pressure, N/m^2
P_L = power drawn by impeller in liquid, W
P_O = headspace pressure, N/m^2
P_S = stagnation pressure, N/m^2
$P(\theta)$ = pressure at any angular location, N/m^2
ΔP_{KE} = frictional pressure drop, N/m^2
ΔP_O = orifice pressure drop, N/m^2
ΔP_P = pressure drop associated with the kinetic energy of the liquid, N/m^2
ΔP_T = total pressure drop, N/m^2
ΔP_σ = pressure drop required to overcome surface tension forces, N/m^2
P_ϕ = pressure of the gas in the dispersed phase, N/m^2
PBTD = pitched blade turbine downflow
PBTU = pitched blade turbine upflow
PJR = plunging jet reactor
PU = propeller upflow
Q_C = rate of gas bubble carriage, m^3/s
Q_E = rate of gas bubble entrapment, m^3/s
Q_G = gas-induction rate in absence of sparging, m^3/s
Q_{GS} = gas-induction rate in the presence of sparging, m^3/s
Q_{SA} = rate of surface aeration, m^3/s
Q_{UG} = rate of accumulation of unreacted gas in headspace, m^3/s
R = impeller radius, m
R_G = universal gas constant
r = radial coordinate, m
r_B = radius of bubble, m
$R_A\underline{a}$ = volumetric rate of reaction, kmol/m^3·s
Re = Reynolds number
S = submergence of impeller in clear liquid, m
SA = surface aerators
SBT = straight blade turbine
Sh = Sherwood number
T = tank diameter, m
T_H = temperature of gas in the holding tank, K
T_{HS} = temperature of gas in the headspace, K
T_ϕ = temperature of gas in the dispersed phase, K
U = liquid velocity, m/s
V = impeller tip velocity, m/s
V_H = volume of gas in the holding tank, m^3
V_{HS} = volume of gas in the headspace, m^3
V_{CG} = liquid velocity at N_{CG}, m/s
V_G = superficial gas velocity, m/s
V_{Gi} = superficial velocity of the sparged gas, m/s
V_i = superficial velocity of the induced gas, m/s
V_L = volume of liquid in dispersion, m^3
V_ϕ = volume of gas in the dispersed phase, m^3

W = blade width, m
X = area of intersection of the vortex with the impeller, m^2
Y = radial distance form the axis, m
z = axial coordinate
z_{GO}, $z_{\phi O}$ = mole fraction of solute gas in headspace and dispersed gas phase

Greek Letters

α = constants
α^* = impeller pumping number, eq 41
β_1, β_2, β_3 = constants in eq 43
ϵ_G = fractional gas holdup
ϵ_S = fractional solid holdup
η = impeller pumping number
λ^* = gas-induction modulus, eq 40, m
μ = viscosity of liquid, Pa·s
μ_W = viscosity of water, Pa·s
ξ_O = fraction of the absorbed oxygen
ρ_G = gas density, kg/m^3
ρ_L = liquid density, kg/m^3
σ = surface tension, N/m
τ = torque, N·m
ϕ = vortexing constant
ω = angular velocity, s^{-1}

Literature Cited

Aldrich, C.; van Deventer, J. S. J. Observations on Induced Aeration in Agitated Slurries. *Chem. Eng. J.* **1994**, *54*, 199−205.

Aldrich, C.; van Deventer, J. S. J. Modelling of Induced Aeration in Turbine Aerators by Use of Radial Basis Function Neural Network. *Can. J. Chem. Eng.* **1996**, *73*, 808−816.

Al Taweel, A. M.; Cheng, Y. H. Effect of Surface Tension on Gas/Liquid Contacting in a Mechanically-Agitated Tank with Stator. *Chem. Eng. Res. Des.* **1995**, *73*, 654−660.

Arbiter, N.; Harris, C. C. Flotation Machines; In *Froth Flotation*; Fuerstenau, D. W., Ed.; AIME: New York, 1962; Chapter 14, pp 347−64.

Arbiter, N.; Steininger, J. Hydrodynamics of Flotation Machines. In *Mineral Processing*, Proceedings of the 6th International Mineral Processing Congress; Roberts, A., Ed.; Pergamon Press: London, 1965.

Arbiter, N.; Harris, C. C.; Yap, R. J. Hydrodynamics of Flotation Cells. *Trans. Soc. Min. Eng. AIME* **1969**, *244*, 134−148.

Baczkiewicz, J.; Michalski, M. Oxygen Transfer During Mixing of Acetic Acid Fermentation Medium with Self-aspirating Tube Agitator. *Proceedings of the 6th European Conference on Mixing*, Pavia, Italy, May 24−26, 1988; BHRA: Cranfield, U.K., 1988.

Barbery, G. Engineering Aspects of Flotation in Minerals Industry: Flotation Machines, Circuits and Their Simulation. In *The Scientific Basis of Flotation*, Ives, K. J., Ed.; NATO-ASI Series; Martinus Nijhoff Publishers: The Hague, 1984; pp 289−348.

Brenner, D.; Freck, M.; McDermott, K.; Post, T. Gas Liquid Mass Transfer of a New Induction Aerator with a Vortex Enhancer; *Proceedings of the 8th European Conference on Mixing*; BHRA: Cambridge, England, 1994.

Calderbank, P. H.; Moo-Young, M. B. The continuous Phase Heat and Mass Transfer Properties of Dispersions. *Chem. Eng. Sci.* **1961**, *16*, 39−54.

Degner, V. R.; Treweek, H. B.; Large Flotation Cell Designs and Development. In *Flotation: A.M. Gaudin Memorial Edition*; AIME: New York, 1976; Vol. 2, Chapter 28, pp 824−31.

Dietrich, E.; Mathieu, C.; Delmas, D.; Jenck, J. Raney-Nickel Catalyzed Hydrogenations: Gas−Liquid Mass Transfer In Gas-Induced Stirred Slurry Reactors. *Chem. Eng. Sci.* **1992**, *47*, 3597−3604.

Doraiswamy, L. K.; Sharma, M. M. *Heterogeneous Reactions: Analysis, Examples, and Reactor Design*; Wiley-Interscience: New York, 1984.

Evans, G. M.; Rielly, C. D.; Davidson, J. F.; Carpenter, K. J. A Fundamental Study of Gas Inducing Impeller Design. In *Fluid Mixing IV*; Institution of Chemical Engineers Symposium Series 121; Institution of Chemical Engineers: Rugby, U.K., 1990; pp 137−152.

Evans, G. M.; Rielly, C. D.; Davidson, J. F.; Carpenter, K. J. Hydrodynamic Characteristics of a Gas-Inducing Impeller. *Proceedings of the 7th European Conference on Mixing*, Kiav, Brugge, Sep 18−20, Belgium; 1991; pp 515−523.

Evans, G. M.; Rigby, G. D.; Jameson, G. J. Influence of Fluid Pressure Field on Gas Flow Rate for a Gas-Inducing Impeller. *Proceedings of the 8th European Conference on Mixing*; BHRA: Cambridge, England, 1994; pp 187−194.

Fallenius, K. A New Set of Equations for the Scale-Up of Flotation Cells. *Developments in Mineral Processing*, Proceedings of the Mineral Processing 13th Congress, 1981; pp 1353−1373.

Flint, L. R. Factors Affecting the Design of Flotation Equipment. *Miner. Sci. Eng.* **1973**, *5*, 232−241.

Forrester, S. F.; Rielly, C. D. Modelling the Increased Gas Capacity of Self-Inducing Impellers. *Chem. Eng. Sci.* **1994**, *49*, 5709−5718.

Forrester, S. F.; Rielly, C. D.; Carpenter, K. J. Bubble Formation from the Moving Blades of a Gas-Inducing Impeller. *Proceedings of the 8th European Conference on Mixing*; BHRA: Cambridge, England, 1994; pp 333−340.

Forrester, S. F.; Rielly, C. D.; Carpenter, K. J. Gas Inducing Impeller Design and Performance Characteristics. *Chem. Eng. Sci.* **1998**, *53*, 603−615.

Grainger-Allen, T. J. N. Bubble Generation in Froth Flotation Machines. *Trans. Inst. Min. Met.* **1970**, *79*, C15−C22.

Harris, C. C. Flotation Machines. In *Flotation: A.M. Gaudin Memorial Edition*; AIME: New York, 1976; Vol. 2, Chapter 27, pp 753−815.

Harris, C. C.; Mensah-Biney, R. K. Aeration Characteristics of Laboratory Flotation Machine Impellers. *Int. J. Min. Process.* **1977**, *4*, 51−67.

Harris, C. C.; Arbiter, N.; Musa, M. J. Mixing and Gangue Dispersion in Flotation Machine Pulps. *Int. J. Miner. Process.* **1983**, *10*, 45−60.

Harris, C. C.; Khandrika, S. M. Flotation Machine Design: Important Hydrodynamic Effects, Slight Geometrical Causes. *Powder Technol.* **1985a**, *43*, 243−48.

Harris, C. C.; Khandrika, S. M. Flotation Machine Design: Impeller Stator Interaction. *Powder Technol.* **1985b**, *43*, 273−78.

Harris, C. C. Flotation Machine Design, Scale-up and Performance: Data Base. In *Advances in Mineral Processing*; Arbiter Symposium; Somasundaram, P., Ed.; Society of Mining Engineers: Littleton, CO, 1986; Chapter 37, pp 618−35.

Heim, A.; Kraslawski, A.; Rzyski, E.; Stelmach, J. Aeration of Bioreactors by Self-aspirating Impellers. *Chem. Eng. J.* **1995**, *58*, 59−63.

Hichri, H.; Accary, A.; Puaux, J. P.; Andrieu, J. Gas−Liquid Mass Transfer Coefficients in a Slurry Batch Reactor Equipped with a Self-Gas-Inducing Agitator. *Ind. Eng. Chem. Res.* **1992**, *31*, 1864−1867.

Hinze, J. O. Fundamentals of the Hydrodynamic Mechanism of Splitting in Dispersion Processes. *AIChE J.* **1955**, *1*, 289,

Hsu, Y.; Chang, H. Onset of Gas Self-Induction and Power Consumption after Gas Induction in an Agitated Tank. *J. Chem. Technol. Biotechnol.* **1995**, *64*, 137.

Hsu, Y.; Huang, C. Characteristics of a New Gas-Induced Reactor. *AIChE J.* **1996**, *42*, 3146.

Hsu, Y.; Huang, K. Effects of Geometrical Factors on Liquid Mixing in a Gas-Induced Agitated Tank. *J. Chem. Technol. Biotechnol.* **1997**, *68*, 222.

Hsu, Y.; Peng, R. Y.; Huang, C. Onset of Gas Induction, Power Consumption, Gas Hold-up and Mass Transfer in a New Gas-Induced Reactor. *Chem. Eng. Sci.* **1997b**, *52*, 3883−3891.

Joshi, J. B. Modifications in the Design of Gas Inducing Impellers. *Chem. Eng. Commun.* **1980**, *5* (1−4), 109−114.

Joshi, J. B.; Sharma, M. M. Mass Transfer and Hydrodynamic Characteristics of Gas Inducing Type of Agitated Contactors. *Can. J. Chem. Eng.* **1977**, *65*, 683−95.

Kastanek, F.; Zahradnk, J.; Kratochvil, J.; Cermak, J. *Chemical Reactors for Gas−Liquid Systems*; Ellis Horwood: New York, 1993 (English edition).

Klassen, V. I.; Mokrusov, V. A. Aeration of Pulp. In *Introduction to the Theory of Flotation*; Butterworths: London, 1963; Chapter 22.

Kingsley, J. P.; Roby, A. K.; Litz, L. M.; Terephthalic Acid Production, U.S. Patent 5,371, 283, 1994.

Koen, C.; Pingaud, B. Development of a Self-Inducing Disperser for Gas/Liquid and Liquid/Liquid Systems. *Proceedings of the 2nd European Conference on Mixing*, Mar 30−Apr 1, 1997; BHRA: Cambridge, England, 1977; Paper F5, pp 67−81.

Levenspiel, O. *Chemical Reaction Engineering*; Wiley Eastern Limited: New Delhi, 1985.

Litz, L. M. Process and Apparatus for Mixing a Gas and a Liquid. U.S. Patent 4,454,077, 1984.

Litz, L. M. A Novel Gas−Liquid Stirred Tank Reactor. *Chem. Eng. Prog.* **1985**, Nov, 36−39.

Litz, L. M.; Weise, M. K.; Adis, M. Gas−Liquid Mixing. U.S. Patent 4,900,480, 1990.

Martin, G. Q. Gas-Inducing Agitator. *Ind. Eng. Chem. Process Des. Dev.* **1972**, *11*, 397−404.

Matsumura, M.; Sakuma, H.; Yamagata, T.; Kobayashi, J. Gas Entrainment in a New Gas Entraining Fermentor. *J. Ferment. Technol.* **1982a**, *60*, 457−462.

Matsumura, M.; Sakuma, H.; Yamagata, T.; Kobayashi, J. Performance of Oxygen Transfer in a New Gas Entraining Fermentor. *J. Ferment. Technol.* **1982b**, *60*, 551−563.

Matsumura, M.; Umemoto, K.; Shinabe, K.; Kobayashi, J. Application of Pure Oxygen in a New Gas Entraining Fermentor. *J. Ferment. Technol.* **1982c**, *60*, 565−578.

Michel, B. J.; Miller, S. A. Power Requirements of Gas−Liquid Agitated Systems. *AIChE. J.* **1962**, *8*, 262−266.

Mundale, V. D. Design of Gas Inducing Type Agitated Reactors. Ph.D. (Technology) Thesis, Bombay University, 1993.

Mundale, V. D.; Joshi, J. B. Optimization of Impeller Design for a Gas Inducing Type Mechanically Agitated Contactor. *Can. J. Chem. Eng.* **1995**, *73*, 161−172.

Patwardhan, A. W.; Joshi, J. B. Hydrodynamics of a Stirred Vessel Equipped with a Gas-Inducing Impeller. *Ind. Eng. Chem. Res.* **1997**, *36*, 3942−3958.

Raidoo, A. D.; Raghav Rao, K. S. M. S.; Sawant, S. B.; Joshi, J. B.; Improvements in a Gas Inducing Impeller Design. *Chem. Eng. Commun.* **1987**, *54*, 241−64.

Rielly, C. D.; Evans, G. M.; Davidson, J. F.; Carpenter, K. J. Effect of Vessel Scale-up on the Hydrodynamics of a Self-Aerating Concave Blade Impeller. *Chem. Eng. Sci.* **1992**, *47*, 3395−3402.

Rigby, G. D.; Evans, G. M.; Jameson, J. G. Influence of a Fluid Pressure Field on the Gas Flow Rate for a Gas Inducing Impeller. *Proceedings of the 8th European Conference on Mixing*; BHRA: Cambridge, England, 1994.

Roby, A. K.; Kingsley, J. P. Oxide Safely with Pure Oxygen; *Chemtech* **1996**, Febr, 39−46.

Saravanan, K.; Joshi, J. B. Gas Inducing Type Mechanically Agitated Contactors: Hydrodynamic Characteristics of Multiple Impellers. *Ind. Eng. Chem. Res.* **1995**, *34*, 2499−2514.

Saravanan, K.; Joshi, J. B. Fractional Gas Hold-Up in Gas Inducing Type of Mechanically Agitated Contactors. *Can. J. Chem. Eng.* **1996**, *74*, 16−30.

Saravanan, K.; Mundale, V. D.; Joshi, J. B. Gas Inducing Type Mechanically Agitated Contactors. *Ind. Eng. Chem. Res.* **1994**, 33, 2226−2241.

Saravanan, K.; Patwardhan, A. W.; Mundale, V. D.; Joshi, J. B. Power Consumption in Gas Inducing Type Mechanically Agitated Contactors. *Ind. Eng. Chem. Res.* **1996**, *35*, 1583−1602.

Saravanan, K.; Patwardhan A. W.; Joshi, J. B. Critical Impeller Speed for Solid Suspension in Gas Inducing Type Mechanically Agitated Contactors. *Can. J. Chem. Eng.* **1997**, *75*, 664−676.

Sawant, S. B.; Joshi, J. B. Critical Impeller Speed for Onset of Gas Inducing in Gas Inducing Types of Agitated Contactors. *Chem. Eng. J.* **1979**, *18*, 87−91.

Sawant, S. B.; Joshi, J. B.; Pangarkar, V. G. Mass Transfer and Hydrodynamic Characteristics of the Wemco Type of Flotation Cell. *Ind. Chem. Eng.* **1980**, *22*, ChE 89−96.

Sawant, S. B.; Joshi, J. B.; Pangarkar, V. G.; Mhaskar, R. D. Mass Transfer and Hydrodynamic Characteristics of the Denver Type of Flotation Cells. *Chem. Eng. J.* **1981**, *21*, 11−19.

Schubert, H.; Bischoffberger, C. On the Hydrodynamics of Flotation Machines. *Int. J. Miner. Process.* **1978**, *5*, 131−142.

Schubert, H. On Some Aspects of the Hydrodynamics of Flotation Processes. 'Flotation of Sulphide Minerals', In *Developments in Mineral Processing*; Forssberg, E., Eds.; Elsevier: Amsterdam 1985; Vol. 6, pp 337−355.

Smith J. M. Simple Performance Correlations for Agitated Vessels. *Proceedings of the 7th European Conference on Mixing*, Brugge, Belgium, Sep 18−20, 1991; BHRA: Cambridge, England, 1991; pp 233−241.

Taggart, A. F. *Handbook of Mineral Dressing*; Wiley-Interscience: New York, 1960.

Tatterson, G. B. *Fluid Mixing and Gas Dispersion in Agitated Tanks*; McGraw-Hill Publishing Co: New York, 1991.

Topiwala, H. H.; Hamer, G. Mass Transfer and Dispersion Properties in a Fermentor with Gas Inducing Impeller. *Trans. Inst. Chem. Eng.* **1974**, *52*, 113−20.

White, D. A.; de Villiers, J. U. Rates of Induced Aeration in Agitated Vessels. *Chem. Eng. J.* **1977**, *14*, 113−18.

Zlokarnik, M.; Judat, H. Tube and Disk Stirrers—Two Efficient Stirrers for the Gassing of Liquids. *Chem. Ing. Technol.* **1967**, *39*, 1163−1168.

Zundelevich, Y. Power Consumption and Gas Capacity of Self-Inducing Turbo Aerators. *AIChE J.* **1979**, *25* (5), 763−73.

Zwietering, Th. N. Suspending Solid Particles in Liquid by Agitators. *Chem. Eng. Sci.* **1958**, *8*, 244−253.

Received for review July 14, 1997
Revised manuscript received September 15, 1998
Accepted September 16, 1998

IE970504E